Summer 8-2019

Computational Fluid Dynamics Analysis of Inverted, Multi-Element Airfoils in Ground Effect

Michael Grabis

Ramesh K. Agarwal

WASHINGTON UNIVERSITY IN ST. LOUIS

McKelvey School of Engineering and Applied Science
Department of Mechanical Engineering and Applied Science

Thesis Examination Committee:
Dr. Ramesh K. Agarwal, Chair
Dr. Spencer Lake
Dr. David Peters

Computational Fluid Dynamics Analysis of Inverted, Multi-Element Airfoils in Ground Effect

by

Michael Grabis

A thesis presented to
The McKelvey School of
Engineering and Applied Science
of Washington University
in partial fulfillment of the
requirements for the degree of
Master of Science

August 2019
Saint Louis, Missouri

Table of Contents

List of Figures

List of Tables

Nomenclature

^{o}	Degrees
α	Angle of attack
c	Chord
C_D	Drag coefficient
C_F	Skin friction coefficient
C_L	Lift coefficient
h	Height above the ground
H1	Two-element airfoil height above ground
H2	Flap vertical spacing, two-element airfoil
H3	Flap horizontal spacing, two-element airfoil
L/D	Aerodynamic efficiency
μ	Viscosity
ρ	Density
Re	Reynolds number
τ_w	Wall shear stress
u_*	Friction velocity
U	Freestream velocity
y	Initial wall cell spacing
CAD	Computer Aided Design
CFD	Computational Fluid Dynamics
NS	Navier Stokes
RANS	Reynolds Averaged Navier Stokes

Acknowledgments

I would like to thank Dr. Ramesh K. Agarwal for his support and guidance from my first ideas to undertake this project to his continuous input and technical guidance throughout the entire process of completing this research.

I would also like to thank the Washington University in St. Louis Formula SAE Team, WashU Racing, for the inspiration to undergo this research project and for all the hard work they put in annually constructing a race car from scratch.

I offer special thanks to the Washington University McKelvey School of Engineering for the opportunity to undertake this research project and the NASA Missouri Space Grant Consortium for the financial support to complete this research.

Michael Grabis

Washington University in St. Louis

August 2019

Dedicated to my family.

ABSTRACT OF THE THESIS

Computational Fluid Dynamics Analysis of Inverted,
Multi-Element Airfoils in Ground Effect

by
Michael Grabis
Master of Science in Aerospace Engineering
Washington University in St. Louis, 2019
Professor Ramesh K. Agarwal, Chair

Formula SAE cars are formula-styled race cars designed to race on an autocross circuit. The autocross circuit is mostly comprised of turning sections as well as a limited amount of straight sections for passing other cars. Highly competitive cars in the competition implement aerodynamic devices to generate negative lift for the race car. This negative lift, or downforce, increases the amount of traction between the race car's tires and the ground ultimately allowing the drivers to turn at faster speeds. Commonly used aerodynamic devices are a front and rear wing; the wing cross sections are defined by configurations of multiple 2D airfoils extruded across the wing's span. This thesis focuses on the research to systematically design the front wing sections of a Formula SAE race car by studying characteristics of high lift, inverted airfoils in ground effect in order to maximize the negative lift. Five high lift, single element airfoils are first studied at multiple angles of attack from which three superior airfoils are chosen and used in a follow-up study that performs flow simulations of these airfoils at various heights above the ground. A second study aims at combining the single-element airfoils into a two-element airfoil configuration to further increase the negative lift by choosing a flap; the flow fields of two-element configurations are computed at various angles of attack and height above the ground, including the vertical and horizontal gap between the main element and the flap. Based on this study, a two-element configuration with a main element and flap is selected to obtain the maximum negative lift.

Chapter 1

Introduction

Formula SAE (FSAE) is an annual student engineering design competition centered on creating a formula-style race car. These cars compete in FSAE competitions world-wide and get evaluated for their design in static events as well as for their performance in dynamic events, the final of which is a 22 km Endurance Race. Competition speeds can be considered low velocity racing; average speeds range from 48 to 57 km/hr while top speeds in a straight-away section can reach around 100 to 105 km/hr [1]. An Endurance lap is mainly comprised of slalom section and turns of various radii, with an additional three straight-away sections that are traditionally used as passing zones. Although the racing is most frequently at a low average velocity, aerodynamics play a large part in vehicular design. Not every vehicle features aerodynamic devices; it is up to the individual team to design, analyze, and test such devices to ensure their implementation is beneficial for the overall performance of the vehicle. This thesis goes through the steps in designing an aerodynamic device for a Formula SAE car, specifically the front wing geometry.

1.1 Motivation

Generally speaking, a car body generates positive lift. Positive lift hinders cornering ability due to a decrease in normal force resulting in a decrease in traction between the vehicle's tires and the ground. This positive lift is usually not an issue with road vehicles, since they do not take tight turns at fast speeds; but this condition greatly impedes a race car's ability to maximize its speed

around a track. Aerodynamic devices can be implemented to negate this positive lift. Many aerodynamic components such as a front wing, a rear wing, a flat underbody tray, and rear diffusers use inverted airfoils to exploit the venturi effect to generate negative lift that decreases the overall positive lift being created by the body, and at some speeds the overall lift coefficient of the car could be negative. Figure 1 shows a side-to-side comparison of a Formula SAE vehicle with (a) having no aerodynamic devices and (b) having a front wing, rear wing, and underbody tray. A FSAE race car can have just an underbody tray, a front wing and rear wing, or all three devices. Just a front or just a rear wing will push the car's center of aerodynamic pressure too far forward or rearward, respectively, and therefore adversely affect the car's dynamic characteristics.

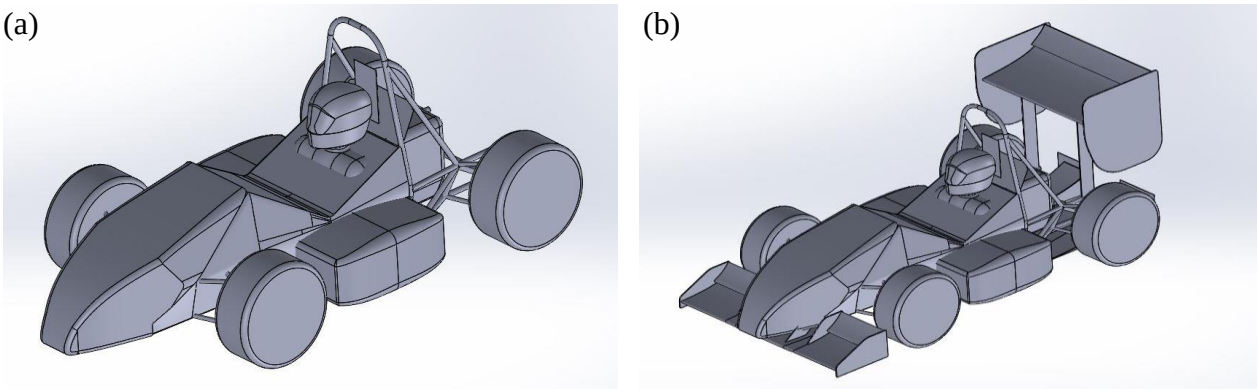

Figure 1 Formula SAE car model (a) without and (b) with aerodynamic devices

A front wing is a logical first design step since it has the most FSAE rules and placement constraints in addition to being the forward-most aerodynamic device on the car that sees the "cleanest" incoming air (not interrupted by any parts of the race car's body). When a satisfactory negative lift coefficient for the front wing is achieved, a rear wing should be designed to couple the forces at the front and rear of the vehicle, effectively pushing the center of pressure towards the rear of the vehicle. This thesis studies several 2D airfoil geometries to maximize the negative lift generation of a front wing attached to Formula SAE car's chassis.

1.2 Current Literature

Airfoils are fundamental aerodynamic geometries that have been used since the creation of early airplanes. The 2D profiles take advantage of a pressure differential caused by splitting air at the leading edge of the airfoil and forcing the air to take two different paths on the top and bottom curves of the airfoil. These two different paths have differences in air velocity; this velocity gradient creates the pressure difference between the top and bottom surfaces of the airfoil in agreement with Bernoulli's principle at low Mach numbers.

Originally published in 1949 and updated in 1957, the Theory of Wing Sections [2] is a compilation of subsonic NACA airfoils, which describes the aerodynamic characteristics as well as concepts of boundary layers, boundary layer control, wings of finite thickness, viscous effects, and high-lift configurations. The high lift generating devices are multi-element airfoils that have retractable trailing edge flaps or leading edge slats for maximizing lift during takeoff and landing. Once the plane is no longer climbing or descending, the slats and flaps can retract in an aerodynamically efficient manner to decrease drag during cruise.

Some of the first documented wind tunnel studies on inverted airfoils were conducted by Zerihan and Zhang. In 2000, they published the study "Aerodynamics of a Single Element Wing in Ground Effect" [3] wherein they studied the Tyrell-26 airfoil in a wind tunnel that had a moving ground. The airfoil was tested at various heights above the ground. They found that as ground height was reduced, higher levels of downforce was generated up to a certain ground height. When the wing is too close to the ground, the flow stalls and the generated downforce is significantly decreased (for ground heights approximately 10% of chord, c, or lower). In 2003, Zerihan and Zhang published another paper titled "Aerodynamics of a Double-Element Wing in Ground Effect" [4]

where they performed a similar experiment as in Reference 3 but added a flap near the trailing edge of the main element. They found that the main element generated the majority of the downforce increasing with a decrease in height above the ground. The addition of a flap decreased the amount of flow separation on the main element and thus further allowed for the generation of additional downforce on the two-element configuration until the flow separated from the flap.

In 2006, Zhang along with Mahon published a paper titled "Computational Analysis of an Inverted Double Element Airfoil in Ground Effect" [5], utilizing the previous two papers to perform numerical simulation through computational fluid dynamic (CFD). The study employed six different turbulence models with Reynolds Averaged Navier-Stokes equations (RANS) to determine the best model to match the wind tunnel results. It was found that the use of the realizable k-ε model gave the best predictions of surface pressure and wake flow field for the airfoil configurations studied at various ground heights. With improvements in CFD practices, some authors have published books, for example by McBeath in 2017 with his 3rd edition of "Competition Car Aerodynamics" [6] which is an excellent attempt towards a practical handbook for aerodynamic studies of race cars. McBeath provides wind tunnel data, and his personal CFD studies to show trends in development of multi-element configurations for race cars and offers insights for addressing various aerodynamics problems for the entire race car such as pressure balance between the front and rear wing at the center of pressure, aerodynamic efficiencies of competition cars, etc.

1.3 Scope of the Thesis

This thesis simplifies the front wing design of an FSAE race car to a 2D planar cross section of a single element or two-element airfoils that are located in close proximity of the ground. Airfoils behave much differently in close proximity of the ground than they do in an unbounded flow; pressure and velocity changes in the flow of air due to the ground are called “ground effects”. The shape of the inverted airfoil close to the ground creates a venturi having an inlet shaped to increase velocity and decrease pressure and an outlet which decreases velocity and increases pressure gradually. A primary goal of this thesis is to study the downforce generation of single element airfoils by increasing the angle of attack (α) on several selected airfoils of $c = 0.33$ m, at a set height above the ground (h). The second part of the single-element study is to vary the airfoils’ h; it is conducted on airfoils with $c = 0.33$ m and the numerically calculated optimal α, $\alpha = 6^{o}$, by varying h. The second goal of this study involves combining the single element airfoil to a flap to create a two-element airfoil configuration to further increase the negative lift of the front wing. The goal of this study is to identify the best geometry for the main element and the flap. For this purpose, simulations are preformed (a) on the main element with varying flap angles, (b) on the two-element airfoil for various heights above the ground, and (c) for various vertical spacings and fore/aft gaps of the flap relative to the trailing edge of the main element.

Chapter 2

Methodology

In this chapter, the geometry, constraints, meshing, and numerical setup for the CFD simulations are discussed. Relevant aspects for the CFD simulation setup are outlined such as the turbulence model used, and the air properties chosen. Computational domains for the single-element and multi-element airfoils are shown including the near wall mesh refinements. The boundary layer parameters including y+ and initial wall spacing are described.

2.1 Geometry

2.1.1 Airfoil Characteristics and Selected Airfoils

Since this study primarily aims at maximizing the negative lift (or downforce) which is generated by single element airfoils and two-element airfoils in ground effect, the most effective way to begin the study is to utilize previously published high-lift airfoils. If previously published airfoils were not chosen, one would have to create altogether new airfoil geometries from scratch, which would significantly extend the research time for an insignificant amount of additional benefit, estimated by the author.

High lift airfoils have many common characteristics, such as large thickness and high camber. Such parameters generally cause additional drag but drag is a penalty that must be paid to generate more downforce. Table 1 shows the selected high lift airfoils and their abbreviated names used in this thesis. Figures 2 and 3 show a superimposed graph of the five airfoils as well as separate contours of airfoils for visual clarity, respectfully.

Table 1 Selected high lift airfoils

Name	Abbreviation
Chuch Hollinger CH 10-48-13	CH10
Eppler E423	E423
Wortmann FX 74-CL5-140	FX74
Liebeck LA5055	LA5055
Selig S1210	S1210

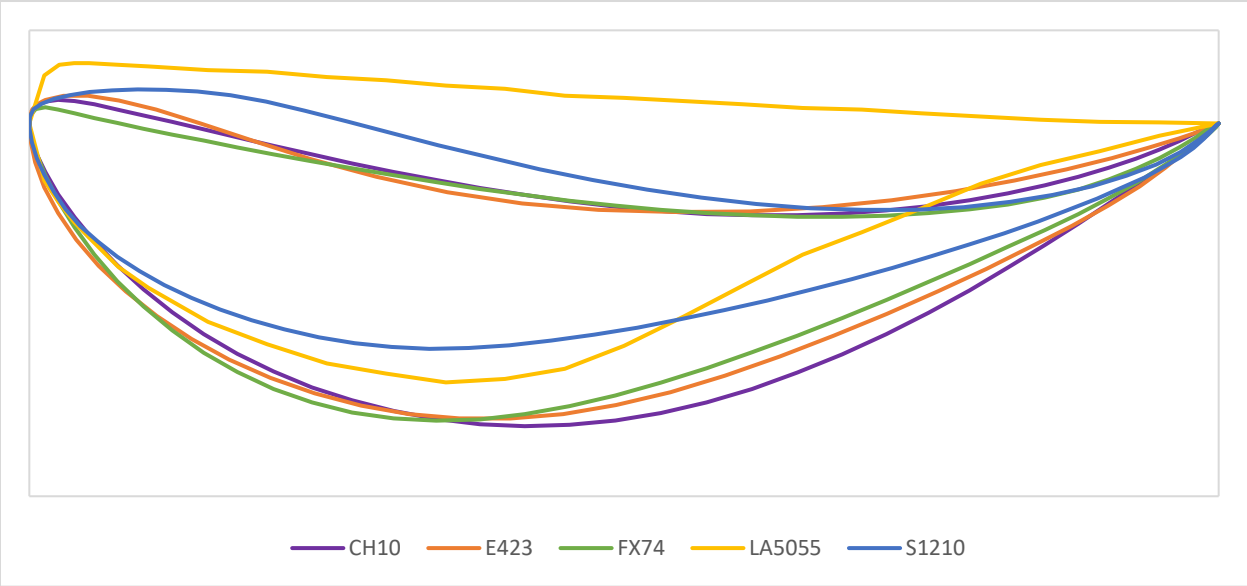

Figure 2 Superimposed airfoil geometries

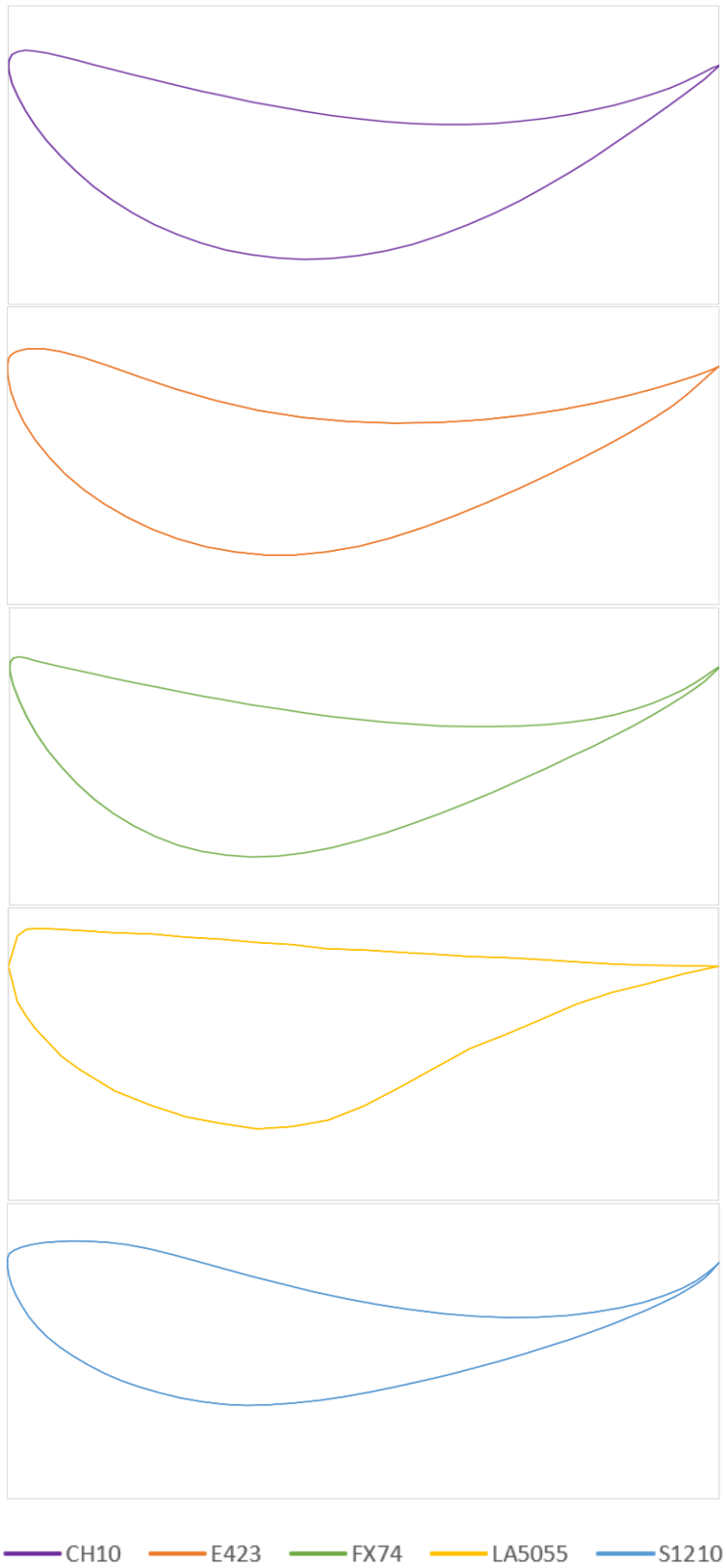

Figure 3 Geometries of various high lift airfoils

2.1.2 Airfoil Geometry Creation

Airfoil geometries, in practice, are defined by sets of coordinate points having x and y positions relative to a common origin. There are numerous databases for finding published airfoil shapes; in this thesis, airfoil coordinates are imported from the UIUC Airfoil Coordinates Database [7]. The UIUC database has over 1,600 different airfoil geometries that are available as .dat files. The database is sorted alphabetically by airfoil name, but each airfoil has a description for common industry use such as subsonic, transonic, supersonic airfoils, or as required in this case, low Reynolds number (Re) airfoils. These files contain the required list of coordinate points for each airfoil, which can be imported into Microsoft Excel for desired formatting.

Solidworks was the computer aided design (CAD) software of choice for manipulating the airfoil points. The Excel points, once formatted into an arrangement that can be read by Solidworks, were imported into the CAD software using the Insert Curve function, "Curve Through XYZ Points". This import took all the individual points that define the desired airfoil and connected them via spline curves that merged the suction and pressure surfaces of the airfoil at the leading and trailing edges. After the airfoil bounding geometry was created, it was scaled to a desired c, and oriented at a desired α, etc. The same was done for the two element airfoils, but the curves for the main element and flap were imported separately so that the software did not confuse the two separate sets of points as if they were a single element airfoil.

The Solidworks airfoil geometries were saved as parasolid files, .x_t, as recommended by ANSYS, to transfer the highest resolution airfoil geometry possible to ICEM. ICEM was chosen as the desired meshing software due to the amount of control the user has to create well-refined structured meshes.

2.1.3 Formula SAE Constraints

Formula SAE has many rules in place to increase the challenge of the design competition as well as to ensure the safety of all participants. There are limitations on the size and location of a front mounted aerodynamic device, most notably that it cannot be "further forward than 700 mm forward of the fronts of the front tires" and "when viewed from the front of the vehicle, the part of the front wheels/tires that are more than 250 mm above ground level must be unobstructed". One must also consider the additional planar area from movement of the tire when the wheel is turned - therefore no part of the wing can enter the "keep-out-zone defined by…positions 75mm in front of and 75mm behind" [1] the front wheel. These rules set a general constraint on sizing and height of potential front wing geometry.

2.2 Mesh Generation

The creation of a high quality grid is of utmost importance for the accuracy of a CFD simulation. Each domain created for a computational fluid dynamics simulation must be properly subdivided into elements that can properly discretize the governing flow equations. As stated prior, the created geometries were imported into the ANSYS meshing software ICEM for its superb ability to allow the user to create a high-quality, structured grid. A structured grid is created by manually creating blocks, which are general regions of mesh refinement, and assigning node quantities to each of the four sides of the block. Once each block edge is subdivided into nodes, each bordering block will have the same horizontal and vertical node quantities to create the desired grid. Refinement can then be added by increasing the number of nodes per edge.

2.2.1 Computational Domains

Instead of a traditional C-Grid that is normally used for airfoil geometries, a rectangular domain was chosen to be able to create a flat surface upstream, downstream, and below the airfoil to capture the ground effect. The bottom of the computational domain under the airfoil was modelled at a h, measured from the lowest point on the airfoil's lower surface, to simulate the ground. The far field outlet boundary was set at 20c downstream of the trailing edge of the airfoil while the far field inlet and far field top boundaries were set at 10c upstream and above of the leading edge of the airfoil, respectively. These distances are standard values that are used in numerous CFD simulations of airfoil flow fields; it is important to distance the far field boundaries of the computational domain far enough away from the airfoil so that the boundary conditions at the stated boundaries remain accurate.

Figures 4 and 5 show the entire computational domain; the flow moves from left to right. The upstream inlet is set as a velocity inlet, the downstream outlet is a pressure outlet, a symmetry plane is used for the top of the domain, and wall conditions are set for the airfoil and the bottom of the domain. The top of the domain is set as a symmetry plane because it functions as a zero-shear boundary that maintains the free-stream velocity boundary condition. In ANSYS Fluent, the wall boundary condition for the airfoil is set as no slip, since the velocity of air is zero right at the edge of the airfoil geometry. The velocity of air is zero due to viscous effects; this creates the boundary layer pressure/velocity gradient. The ground boundary condition was set as a moving wall to replicate a moving ground beneath the race car with a velocity set to 14.6 m/s to match the free-stream velocity.

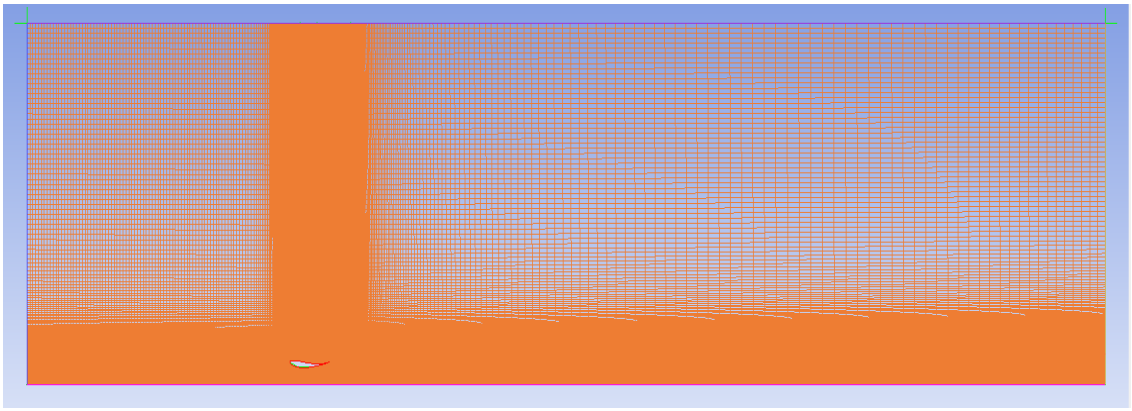

Figure 4 Computational domain for the single-element airfoil

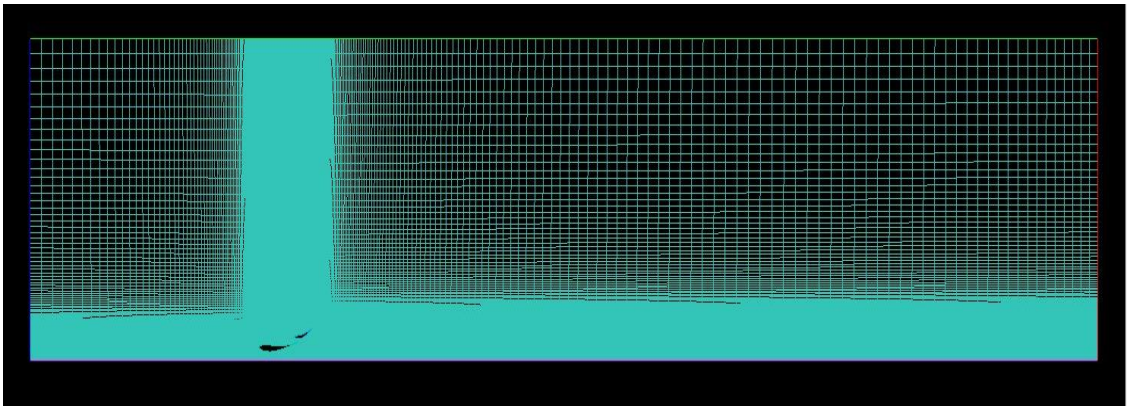

Figure 5 Computational domain for the two-element airfoil

2.2.2 Near Wall Mesh Refinement

Since the airfoil and ground have boundary layers, it is necessary to refine the grid close to them to achieve an accurate calculation of the flow field. In CFD, the cell spacing of the first mesh point from a solid surface is called the y+ value; each turbulence model requires a slightly different y+ value to accurately calculate the viscous sublayer of a turbulent boundary layer. In the presented simulations, a SST k-ω turbulence model is used (more information on CFD numerical setup and turbulence modelling is given in Section 2.3); therefore grid spacing of the first mesh point off the wall was chosen such that y+ <1 to accurately capture the near wall region of the boundary layer.

The following equations describe how the initial cell spacing is calculated; this process is given in the CFD-Online website [8]. First, the Re is calculated from Equation 1.

$$\mathrm{Re} = \frac{\rho * U * c}{\mu} \tag{1}$$

Using air properties defined in Section 2.3.2, a chord set to c = 0.33 m, Re is found to be approximately 330,000. The skin friction coefficient is calculated from Equation 2.

$$C_F = [2 * \log(\mathrm{Re}) - 0.65]^{-2.3} \tag{2}$$

Using the Re calculated from Equation 1, C_F is found to be 0.00459. Knowing the skin friction, the wall shear stress can be calculated from Equation 3.

$$\tau_w = C_f * \frac{1}{2} * \rho * U^2 \tag{3}$$

Using the C_F found from Equation 2, the wall shear stress is approximately 0.600 Pa. The wall shear stress is used to find the friction velocity from Equation 4.

$$u_* = \mathrm{sqrt}\left(\frac{\tau_w}{\rho}\right) \tag{4}$$

Using the τ_w found from Equation 3, the friction velocity is determined as 0.700 m/s. The friction velocity is the last value needed to find the initial cell spacing off the wall. For a desired y+ value of 1, and using the calculated friction velocity, Equation 5 shows that the spacing of the first grid point from the wall can be obtained as:

$$y = \frac{y^+ * \mu}{\rho * u_*} \tag{4}$$

The initial wall cell spacing (y) is found to be 0.00002 m and is used here for both the single and two element cases. Figures 6 and 7 respectively show the mesh refinements for the single element and two-element airfoils.

In the near-wall refinements, the structured grid is generated so as to be able to slowly increase the mesh spacing from the initial wall spacing of the first grid point from the wall (a growth rate between 1.05-1.1 between cells) to a point where the mesh is coarse enough to step up to a growth rate of around 1.5-2.

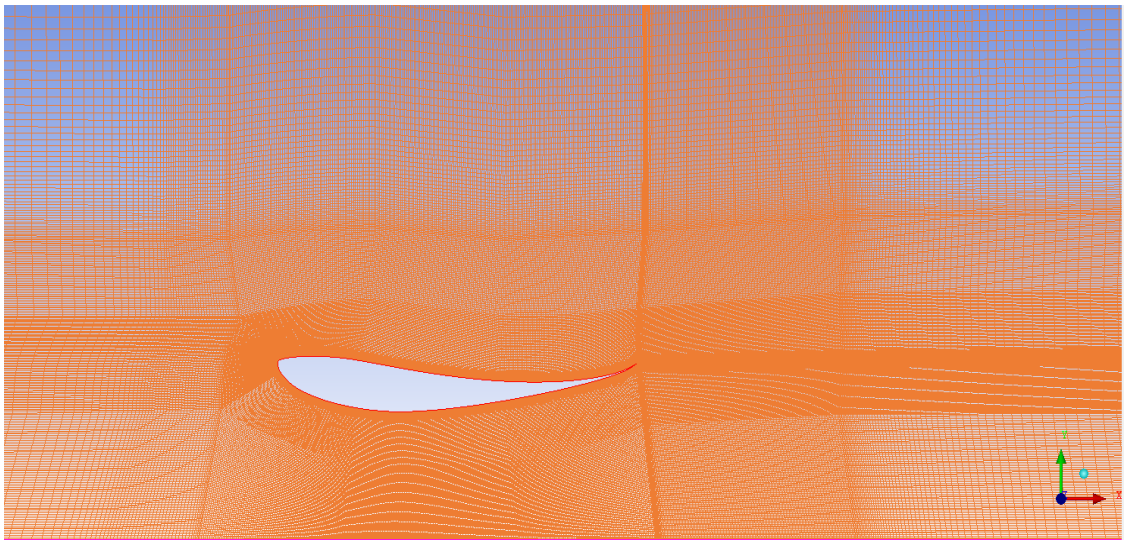

Figure 6 Near-field mesh for the single element airfoil

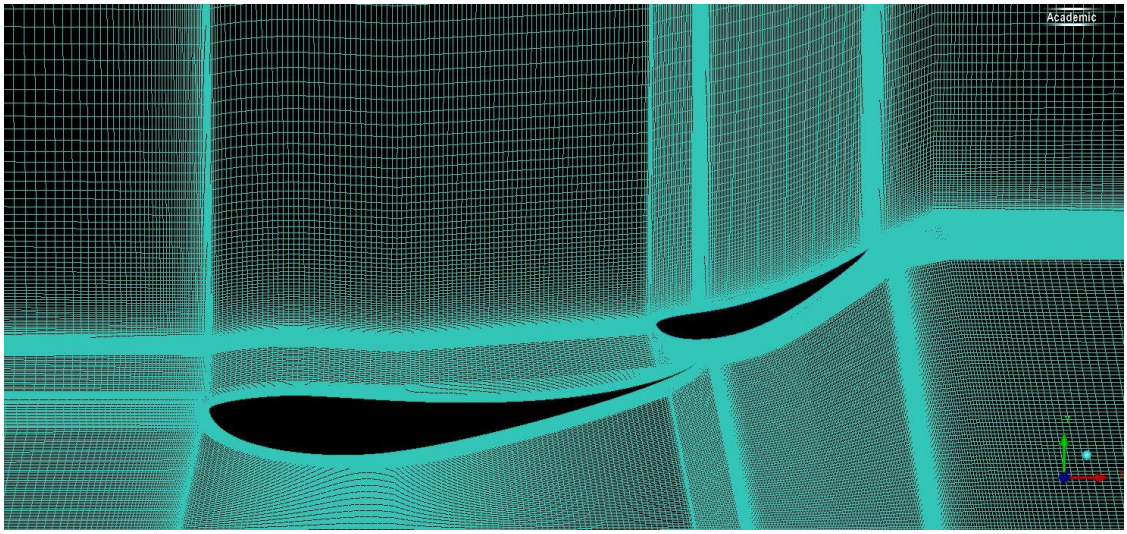

Figure 7 Near-field mesh for the two-element airfoil

2.2.3 Mesh Independence Study

A mesh independence study was conducted to determine the accuracy of the solution for various mesh densities; a solution that is mesh independent is the one that does not change with additional mesh points. A mesh independence study is necessary in a simulation to obtain an accurate solution by using the fewest number of elements in a grid. Using the minimum number of cells to accurately converge a solution is convenient due to faster simulation run times. A rule of thumb can be used that each time a number of cells is doubled; the simulation time is also doubled. The mesh independence study was conducted for the simulation of the single element CH10 airfoil at $\alpha = 0^o$ and h = 0.106 m using three mesh densities. The results are shown in Table 2.

Table 2 Mesh independence study for three mesh densities.

Elements	C_D	C_L
150,000	0.04372	-1.11125
250,000	0.04371	-1.11307
350,000	0.04370	-1.1131

It can be seen from Table 2 that the values for C_D and C_L do not vary significantly using different mesh densities. A mesh density of 150,000 therefore was chosen to decrease the overall run time of simulations. For the two-element case, since the combined c increases from 0.33 m to 0.5 m, a mesh density of 180,000 cells was chosen in order to adequately refine the geometry around the flap while still maintaining a similar mesh density around both elements as was for the single-element case. This allows for a coarse mesh spacing in the far field where there are minute changes in flow velocity or pressure.

2.3 CFD Simulations

ANSYS Fluent was the numerical solver of choice for the flow simulations. The 2D airfoil meshes were converted from structured to unstructured meshes and then output from ICEM with their respective proper boundary conditions into Fluent. For the general setup of the simulation, a pressure-based solver was utilized due to the low Mach number and therefore nearly incompressible nature of the flow. This selection does not take into account any acoustic time scales and therefore reduces the computational effort of each simulation leading to quicker solution convergence since the timestep for the pressure based solver is purely calculated based on the flow velocity. A steady state finite-volume solver in Fluent is employed for the solution of the Reynolds Averaged Navier-Stokes (RANS) equations.

2.3.1 Turbulence Model

SST k-ω turbulence model was chosen for the solution of incompressible RANS equations. The RANS equations are the most commonly used turbulence modelling equations; they are time-averaged model of Navier-Stokes equations (NS) that take into account Reynolds decomposition of flow variables in time-averaged mean quantity and its fluctuating part. NS equations are linear momentum conservation equations that involve a convection term and a diffusion term along with pressure, viscous, and body forces; hence they have the ability to model turbulent viscous flow [9]. Due to the low velocity of the simulations, a low-Re correction was also employed with the turbulence model.

A second-order upwind scheme was used for discretization of convection terms and the diffusion terms were second-order central-differenced. SIMPLE algorithm was used for pressure-velocity coupling. First-order spatial discretization of convection terms was used for first 1000 iterations to speed up the convergence. After that, the second-order upwind algorithm was turned on until solution convergence was achieved. Convergence was achieved in approximately 8-10,000 iterations with residuals for all the governing equations and flow variables reaching at least 1e-5.

2.3.2 Air Properties

The flow inlet speed was set at 14.6 m/s (chosen from the average speeds stated in the FSAE rules) and the ground boundary condition was set as a moving wall (mimicking a moving ground) with a velocity set to 14.6 m/s. Since this is a low Mach number flow (M << 0.3), the flow is approximated as incompressible and the air is treated as an ideal gas. Additional properties of the air with units are given in Table 3.

Table 3 ANSYS Fluent air properties

Properties	Values
Density (ρ)	1.225 kg/m^3
Specific Heat (c_p)	1006.43 J/kg-K
Thermal Conductivity	0.0242 W/m-k
Viscosity (μ)	1.789 x 10^{-5} kg/m/s
Molecular Weight	28.966 kg/kgmol

Chapter 3

Single Element Airfoil Numerical Results

Two studies were conducted on several single element airfoils. The goal of the first study was to determine the optimum α and that of the second study to determine the optimal h for the best performance in terms of maximum negative lift or downforce. The first single element study was conducted on airfoils with c = 0.33 m at varying angles of attack with a constant height above the ground of h = 0.106 m. The flow field for each airfoil was computed for $\alpha = 0^o$ to 15^o in increments of 3^o. It was decided that this range of angles of attack for the main element of an FSAE front wing are reasonable based on the rule constraints. Additionally, the upper bound of α is where the flow begins to separate from the trailing edge of the airfoils.

The second study to determine an optimal h, was conducted to determine how the ground proximity affects the flow field of an airfoil at a low Re. The three airfoils having the largest $-C_L$ values from the first study were chosen for this study to reduce overall computational effort. In this study, $\alpha = 6^o$ was chosen while h was varied from 0.0127 m to 0.9144 m, with smaller changes in height between runs when the airfoil was closer to the ground to increase data resolution.

3.1 Simulation Validation

Since there will be no wind tunnel testing completed for the optimized front wing geometry, an accepted method for ensuring the real-world accuracy of the simulation is to calibrate the CFD

methodology employed to a previously published result. This thesis uses the CFD simulation results from the paper "Numerical Investigation of the Aerodynamics of an Inverted Three Element Airfoil in Ground Effect for a Race Car Application" [10] that validated their numerical results against the experiment of Zerihan and Zhang [3]. Zerihan and Zhang conducted wind tunnel studies on the Tyrell-026 airfoil in ground effect; Qu et al. reproduced the published experimental results for the Tyrell-026 airfoil at h/c = 0.224 using a CFD simulation. They later went on to use that same methodology for studying the three-element 30P30N airfoil in close proximity to the ground to determine the downforce generated by this configuration. This thesis takes the numerical data published by Qu et al. for the 30P30N airfoil in ground effect; the pressure coefficient along the x-axis at h/c = 0.5 is plotted in Figure 8. There is excellent agreement between the published and present results; using the simulation methodology described in Section 2.3. The same validated methodology is used in all single and two-element airfoil simulations reported in this thesis.

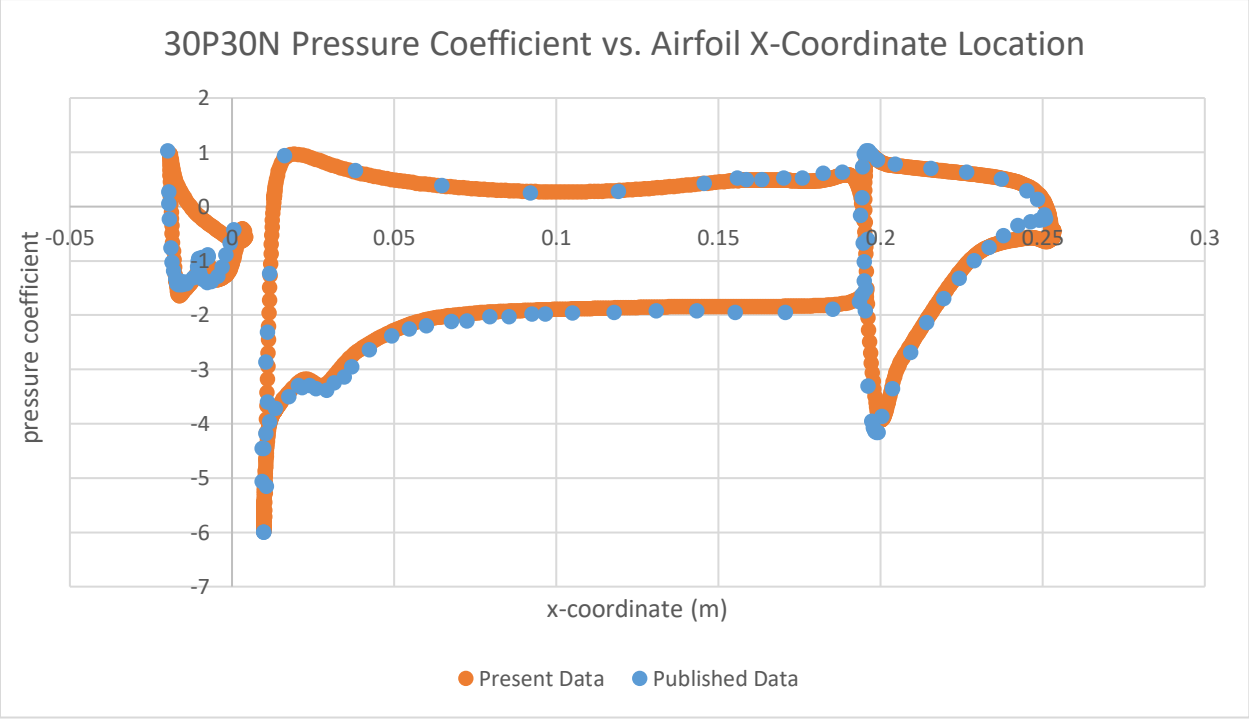

Figure 8 Validation of present CFD methodology using the 30P30N three-element airfoil in ground effect

3.2 Single Element Airfoil Angle of Attack

The Re in these simulations is approximately 300,000 (calculated by using Equation 1), assuming air properties at sea level (Table 3) and a freestream velocity of 14.6 m/s. The reference c for the single element airfoils is 0.33 m. The primary goal of this study is to determine which airfoils have the highest C_L and at which angles of attack that peak value occurs. It is required for the airfoils to be in ground effect, so the height above the ground is arbitrarily set at h = 0.106. Figure 9 shows how changes in α affect the negative lift coefficient of each of the five airfoils considered and Figure 10 shows how changes in α affect the drag coefficient for each airfoil.

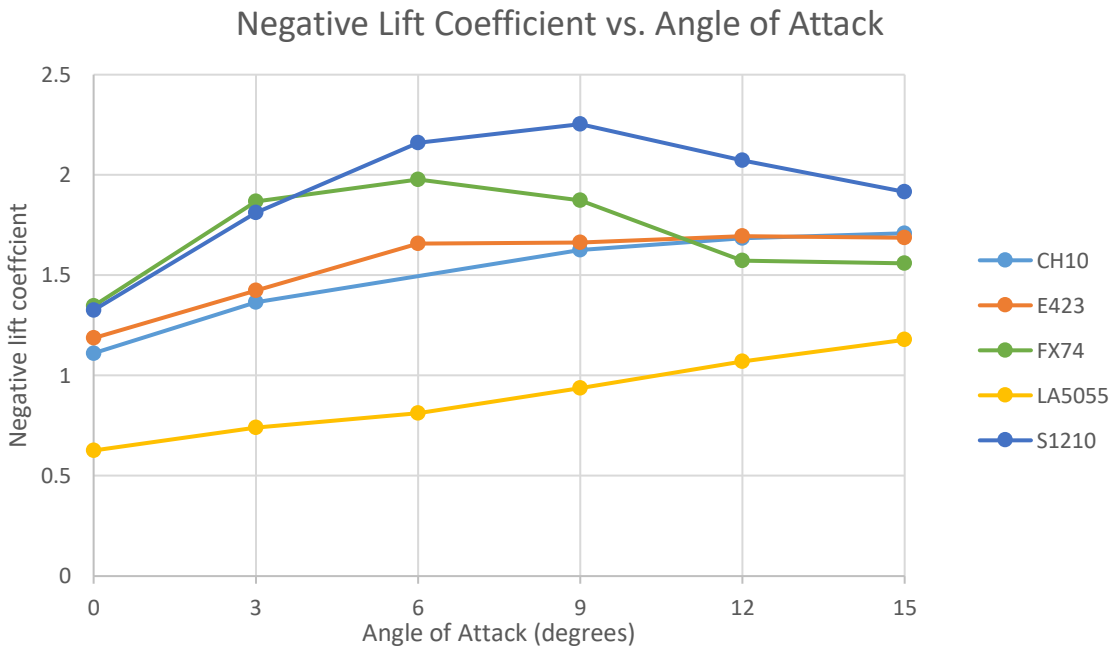

Figure 9 Computed negative lift coefficient of various airfoils at various α

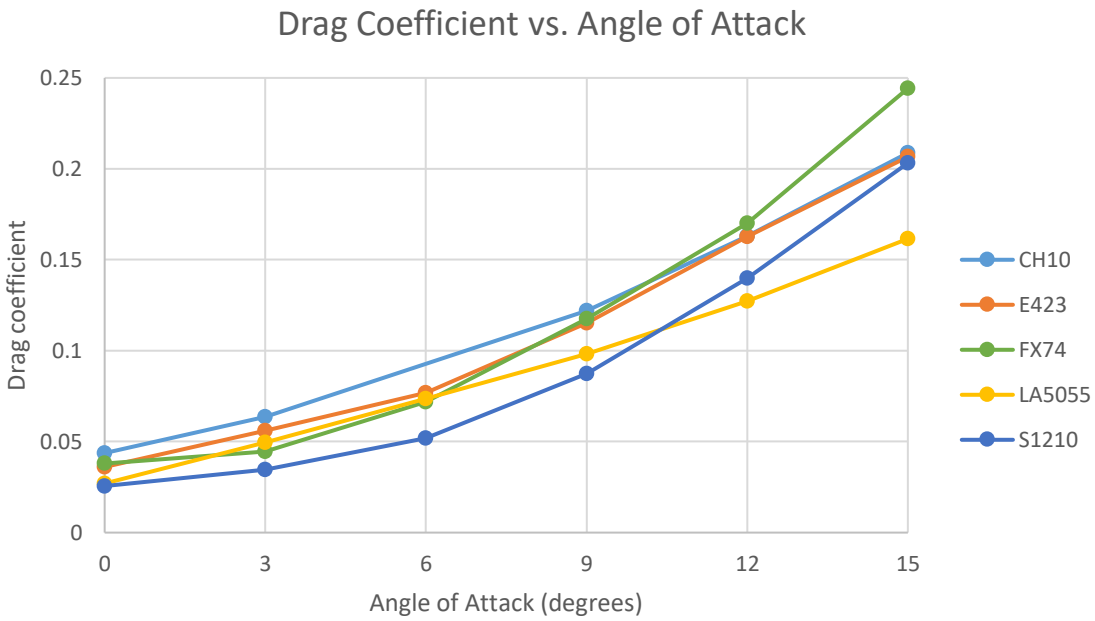

Figure 10 Computed drag coefficient of various airfoils at various α

It can be noted from Figs. 9 and 10 that there is much greater variation in the lift coefficients of different airfoils than in their drag coefficients. The CH10, E423, FX74, and S1210 airfoils all have relatively high negative lift coefficients between 3° and 9°. It is difficult to evaluate the performance of an airfoil by directly comparing the drag to the negative lift coefficient; therefore in Figure 11 a plot of the airfoil efficiency is introduced to determine which airfoils are aerodynamically most efficient (with greater C_L/C_D). Drag is not an important factor at average Formula SAE speeds (14.6 m/s); negative lift generation is of much greater importance in the airfoil selection, nevertheless it is still useful to see the overall airfoil efficiency in selecting an airfoil. Efficiency can be a deciding factor in airfoil selection if two airfoils generate similar amounts of negative lift.

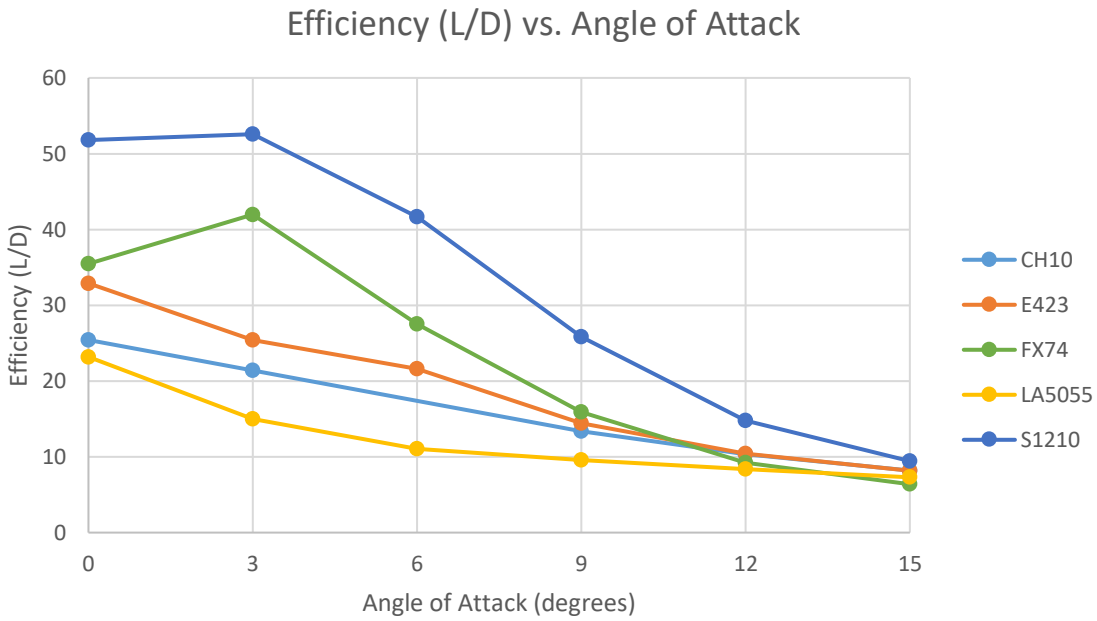

Figure 11 Computed L/D of various airfoils at various α

From Figure 11, it is evident that the S1210 airfoil is superior for the main element of a Formula SAE car front wing. It generates the highest amount of negative lift as well as has the highest efficiency (L/D) for every α considered. Figure 12 shows the velocity magnitude contours around inverted S1210 airfoil between $\alpha = 6^{o}$ and $\alpha = 15^{o}$. These contours show the change in the velocity field as the α increases; this change is responsible for decreasing the L/D as the α increases resulting in increased flow separation.

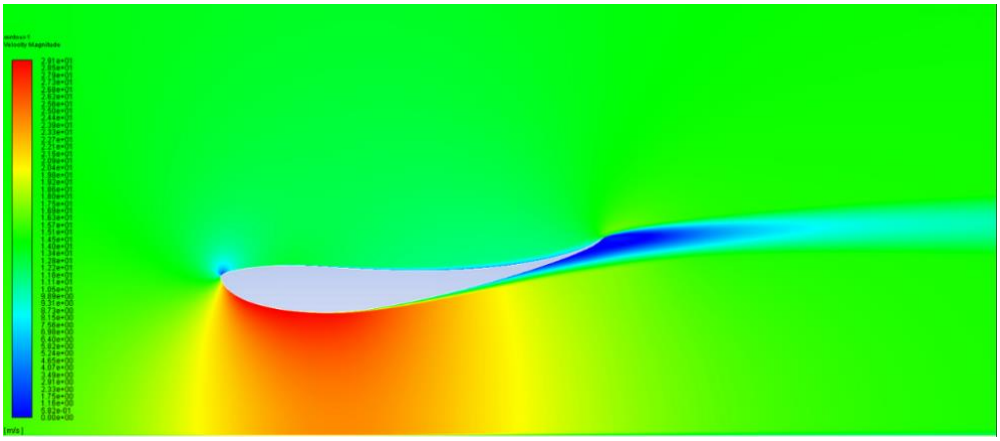

(a) α = 6º

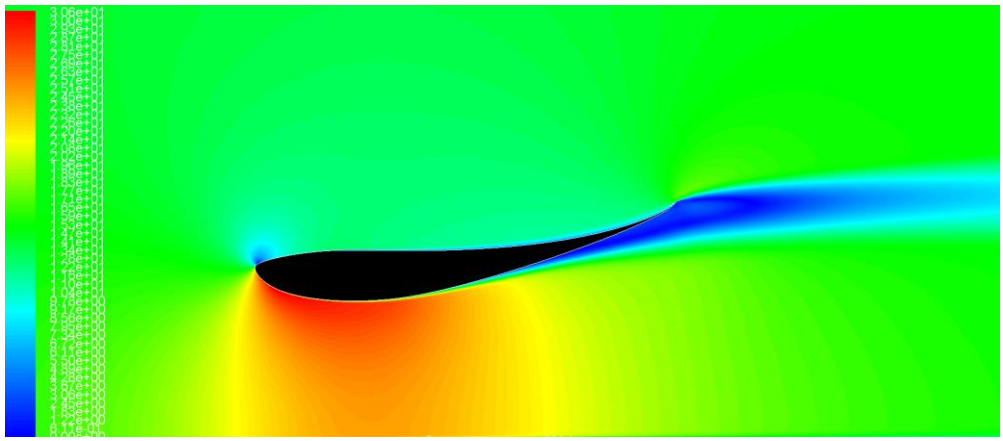

(b) α = 9º

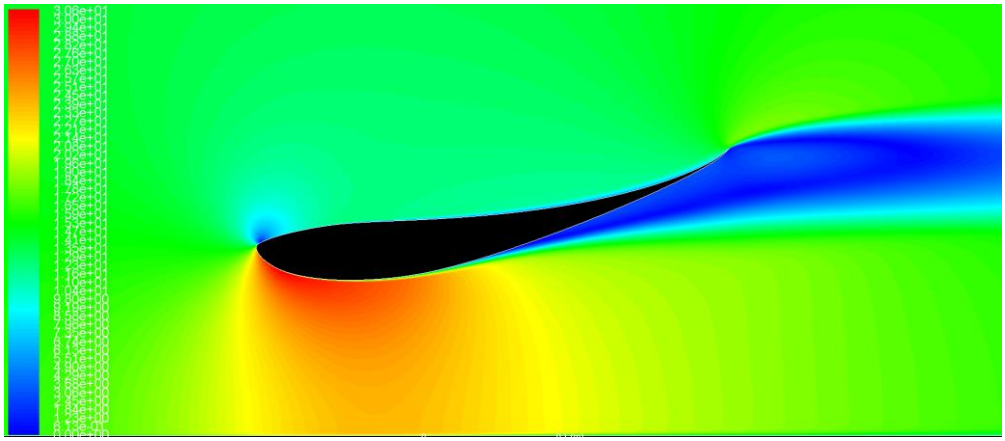

(c) α = 12º

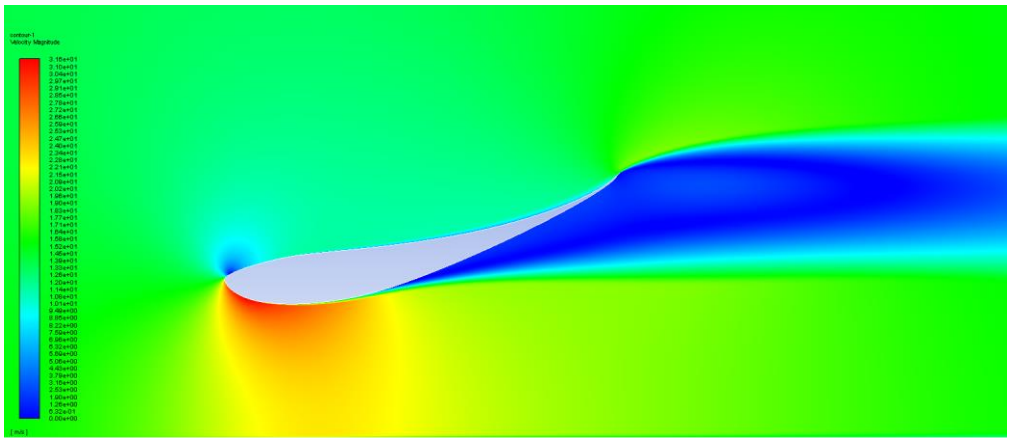

(d) α = 15º

Figure 12 Velocity contours around S1210 airfoil at various α

The areas of high velocity in Figure 12 are highlighted in colors ranging from yellow to red; free-stream air velocity is green, while lowest velocity regions are colored from light to dark blue. For the S1210 airfoil, the negative lift generation peaks between $\alpha = 6^o$ to 9^o and then begins to drop. The increasingly larger areas of dark blue in Figure 12 shows the stall (increased flow separation from the trailing edge of the airfoil) at higher angles of attack. Based on the Bernoulli's principle, as velocity increases the pressure decreases and vice versa, thus the greater velocity region seen in Figure 12(a) and 12(b) creates a larger, lower-pressure area on the bottom surface of the airfoil contributing to an increased amount of negative lift. The flow separation impedes the airfoil's ability to create a low-pressure region, thus it can be seen from Figure 9 that the negative lift generation begins to decrease as the separation region on the bottom surface of the inverted airfoil increases with increase in α.

3.3 Single Element Airfoil Heights Above the Ground

As shown in Section 3.2, the S1210, FX74, and E423 airfoils are able to generate the largest amounts of negative lift and are the three most efficient airfoils with the highest L/D. These three airfoils are selected for this second study that involves varying the h. This study is useful in understanding how the ground effect plays a role in Formula SAE race car aerodynamics. To understand the effect of h, $\alpha = 6^o$ is used in this study and all the three airfoils are simulated at the same speed with same c as employed in the first study, Section 3.2. Figure 13 shows the changes in negative lift coefficient and drag coefficient relative to changes in h.

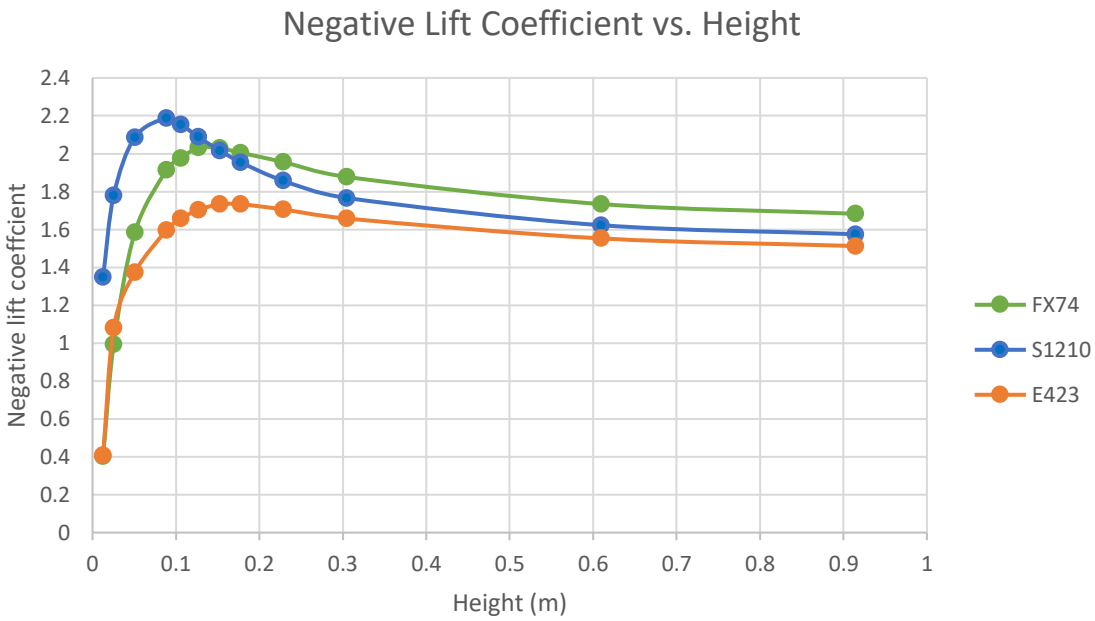

Figure 13 Negative lift coefficient of three airfoils at various h, $\alpha = 6^{o}$

From Figure 13, it can be seen that the 2D airfoils in closest proximity to the ground do not generate the highest amounts of negative lift. Many studies from literature state that downforce increases with a decreased h, but when the airfoil is in very close proximity to the ground, the trend begins to reverse. The S1210 airfoil has the highest negative lift between h = 0.0127 m and 0.1524 m; on the other hand, the lift generated by the FX74 from 0.1542 m to the maximum h = 0.9144 m is greater than that of the S1210 airfoil. This result provides a very useful insight since a rear wing must be created to balance the pressure and force effects of the front wing on Formula SAE vehicle and therefore the FX74 airfoil would be a rational choice over the S1210 airfoil for main element of the rear wing. The peak lift generation for the S1210 airfoil is at h ~ 0.0889 m, therefore ideally the front wing main element should be positioned at this height to have the largest negative lift generation or downforce.

Figure 14 shows the relationship between drag coefficient and height above the ground. The airfoils in closest proximity to the ground have an exponentially higher (R^2 = 0.942) drag coefficient.

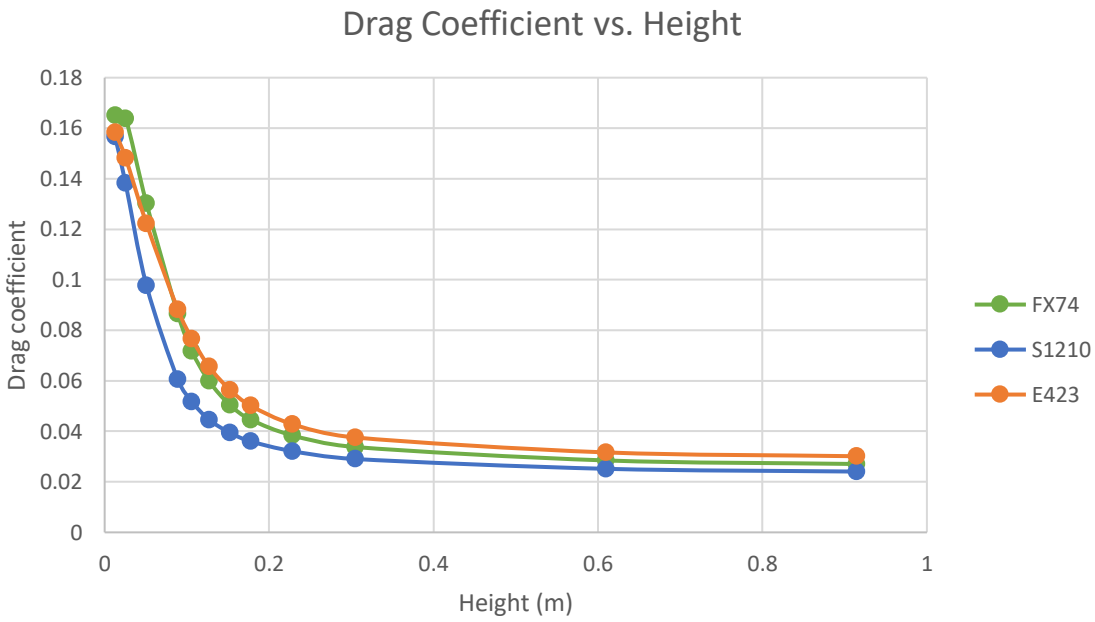

Figure 14 Drag coefficient of three airfoils at various h, $\alpha = 6^o$

It is interesting to note that for h above 0.3 m, the lift and drag coefficients begin to plateau. This value is approximately at h/c of 1. The reason the values for lift and drag reach a plateau is that the ground no longer has a significant effect on the flow fields of the airfoils. This fact can be observed by examining Figure 15, which shows the velocity contour plots for the S1210 airfoil at various h. In the closest ground proximities, as shown in Figure 15(a) and Figure 15(b), there is significant flow separation close to h = 0.0127 m and 0.0508 m, which significantly reduces the downforce generated by the airfoil. At these small h values, there is boundary layer interference between the airfoil and the ground. After the C_L peaks, close to h = 0.1 m, the flow separation does not occur and the venturi effect due to the close ground proximity quickly diminishes.

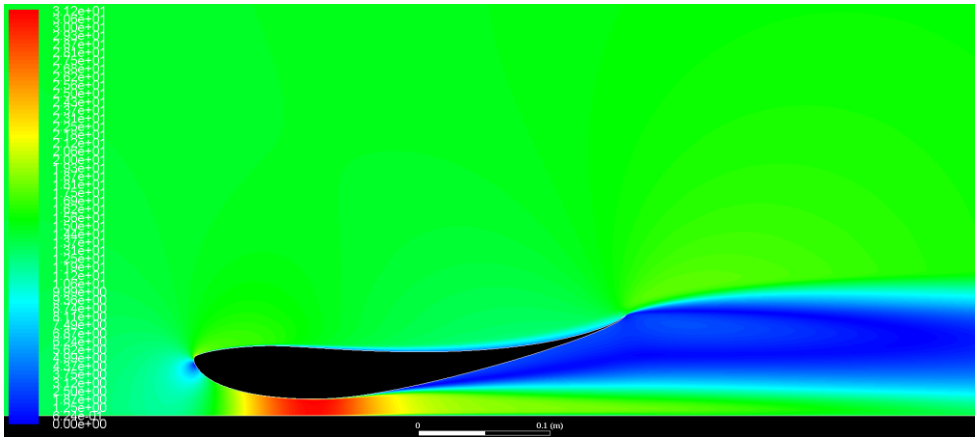

(a) h = 0.0127 m

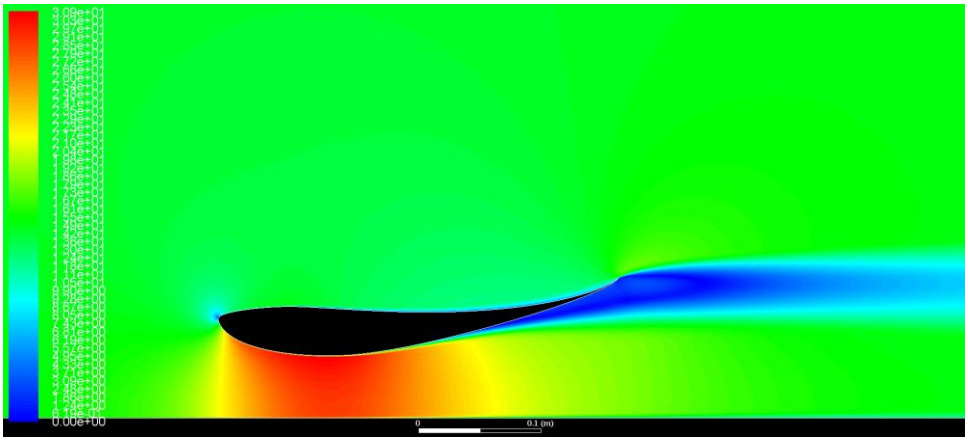

(b) h = 0.0508 m

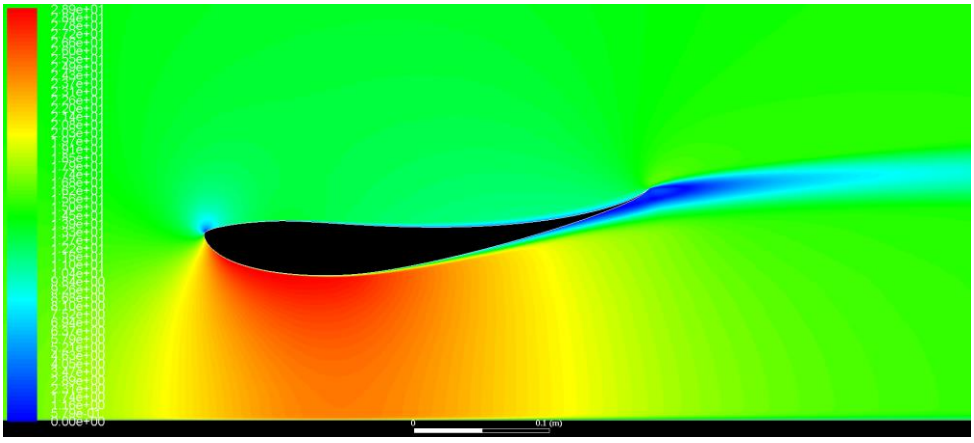

(c) h = 0.1060 m

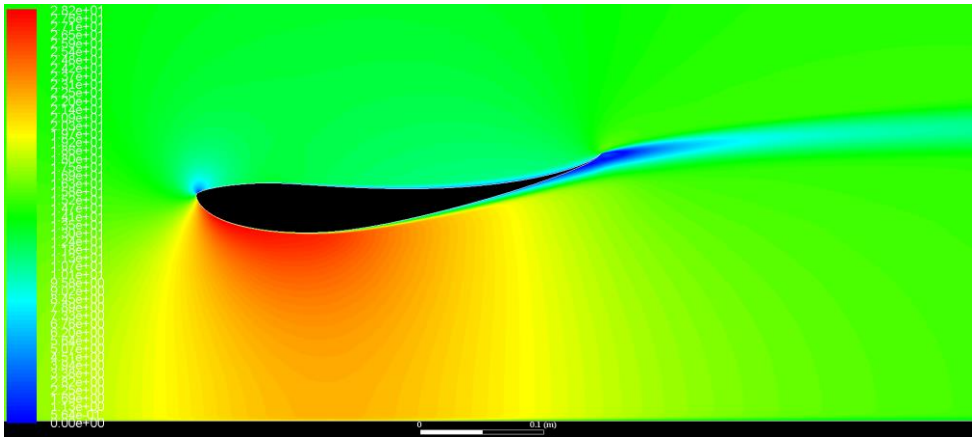

(d) h = 0.1524 m

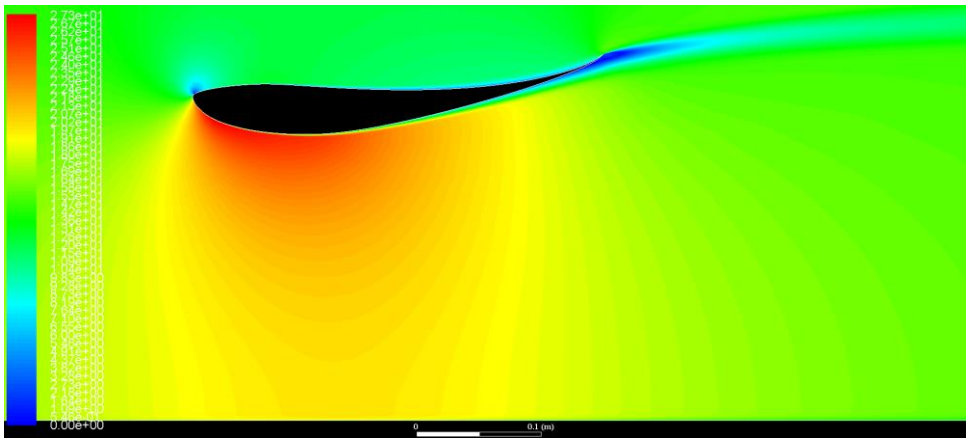

(e) h = 0.2286m

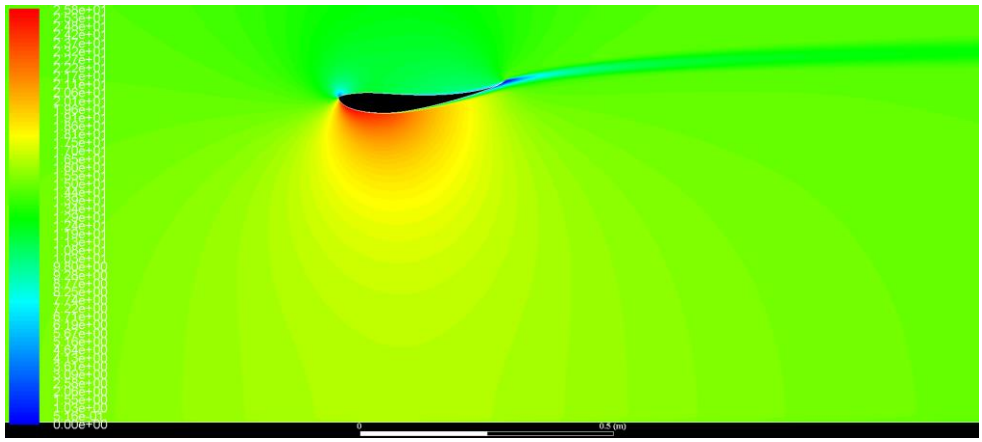

(f) h = 0.6096

Figure 15 Velocity contour plots for the S1210 airfoil at various h

An efficiency (L/D) comparison of the three airfoils is given in Figure 16.

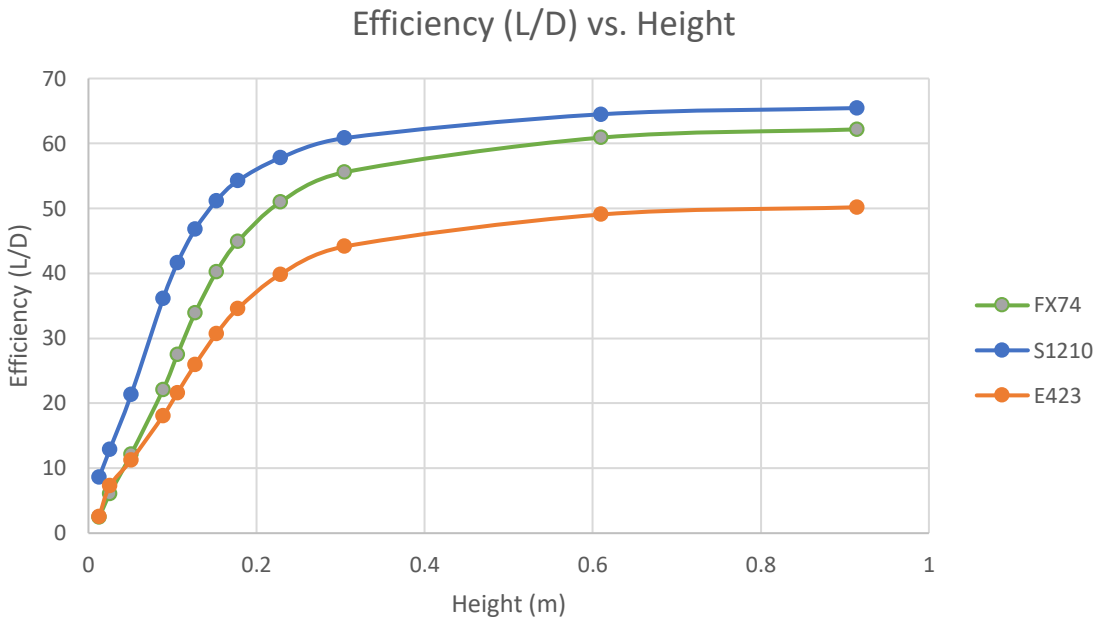

Figure 16 Computed L/D of three airfoils for various h

Again, it can be seen from Figure 16 that the S1210 airfoil has the highest value of L/D at various heights above the ground; it also has the highest value of negative lift in close proximity to the ground as shown in Figure 13. Based on this study, the S1210 airfoil is the airfoil of choice for the front wing main element of the Formula SAE race car being designed by the Formula SAE Team at Washington University - WashU Racing. The inverted S1210 airfoil will be positioned at α between 6^{o} and 9^{o} and at h between 0.0508 m and 0.0889 m, based on this study.

Chapter 4

Two Element Airfoil Numerical Results

This chapter builds on the single element airfoil studies described in Chapter 3 by combining the S1210 main element airfoil with a second element, commonly referred to as a flap. The flap is located vertically just above the trailing edge of the main element. The two-element study is conducted with the main element of c = 0.33 m; if a larger c is desired in future applications, the c value can be changed; however the relationship between the height (h) and chord (c), that is h/c, must be scaled by the amount by which the c is increased. The main element is set at h = 0.0508 m, and $\alpha = 6^{o}$.

A brief background on flap function is provided here. There are four main effects that the flap has on the main element; these are the circulation effect, dumping effect, off-the-surface pressure recovery, and fresh-boundary layer effect [11]. The circulation effect occurs because the trailing edge of the flap is in the high velocity wake from the main element, which in turn induces larger circulation on the main element. Off-the surface pressure recovery increases the effective area in which the higher velocity flow decreases in speed (similar to a diffuser); thus, the flap efficiently decelerates the wake from the main element. The dumping effect takes advantage of the boundary layer on the flap decreasing the pressure/velocity gradient from the trailing edge of the main element thereby delaying flow separation. The fresh boundary layer effect is advantageous since the flap boundary layer is not influenced by the freestream until the air is shed from the main

element. A thinner boundary layer on the flap will be able to withstand larger adverse pressure gradients; this is the case since the velocity of the flow around the flap is greater than the main element.

The three high-lift airfoils were employed as flap geometries; each had a chord c = 0.1524 m (about 40% c of the main element). This ratio was decided from the Competition Car Aerodynamics reference [6]. McBeath conducted a study on chord ratios between the main element and flap sizing, determining that about a ratio of 0.4c is desirable for this application. The lowest point on each flap was 0.015 m above the trailing edge of the main element (roughly 5% of the total c of the two-element airfoil); this ratio was also used by McBeath. The two element studies include selection of flap geometry, main element and flap α, flap vertical spacing above the main element, and the flap fore/aft or horizontal spacing relative to the main element.

4.1 Main Element Airfoil and Flap Pairing

Having selected the S1210 airfoil as the main element of the front wing of formula SAE race car based on the simulations in Chapter 3, the first two-element configuration study was conducted to determine the superior airfoil geometry for the flap. Three airfoils (S1210, FX74 and E423) with highest values of downforce were selected for the flap geometries for the two element airfoils. The flap c is set at 0.1524 m, which is about 1/3 of the combined c of approximately 0.5 m, a desirable size found from literature. Flap α was varied from 20^o to 50^o to determine how the second element affects the main element flow field using the same flow parameters used in single element studies in Chapter 3. Figures 17 - 19 show the negative lift coefficient, drag coefficient, and efficiency of the two-element configuration. The legend in these figures, e.g. S1210 6 deg, S1210 implies that the main element is the S1210 with $\alpha = 6^o$ and the flap airfoil is the S1210 airfoil.

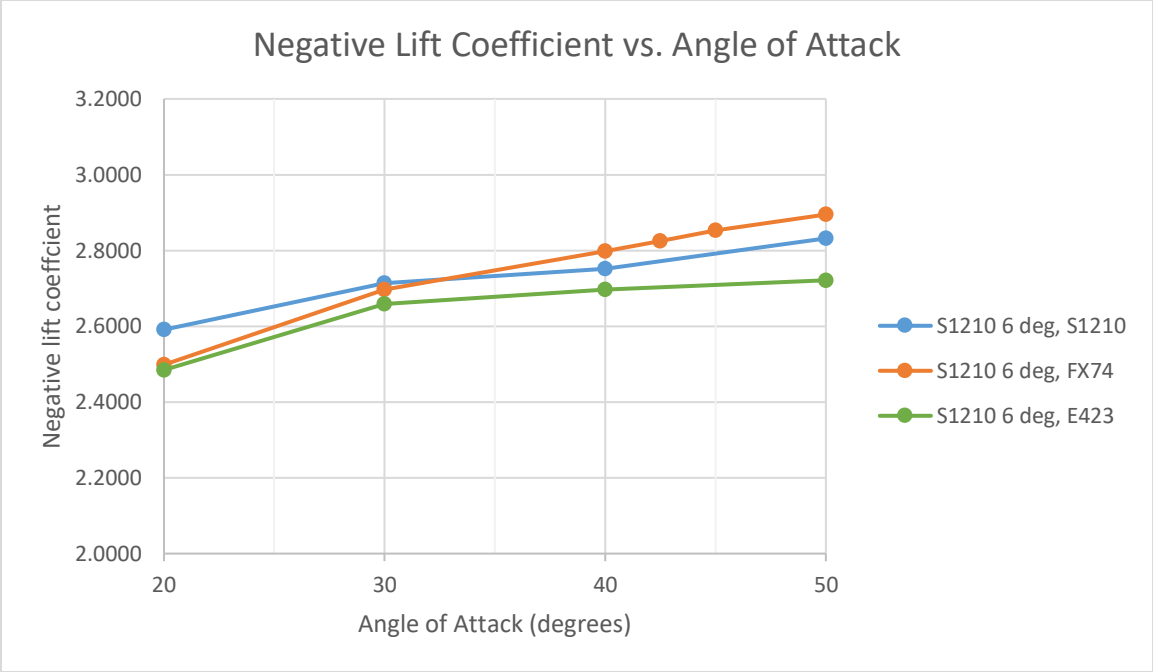

Figure 17 Computed negative lift coefficient of two-element airfoils at various flap α

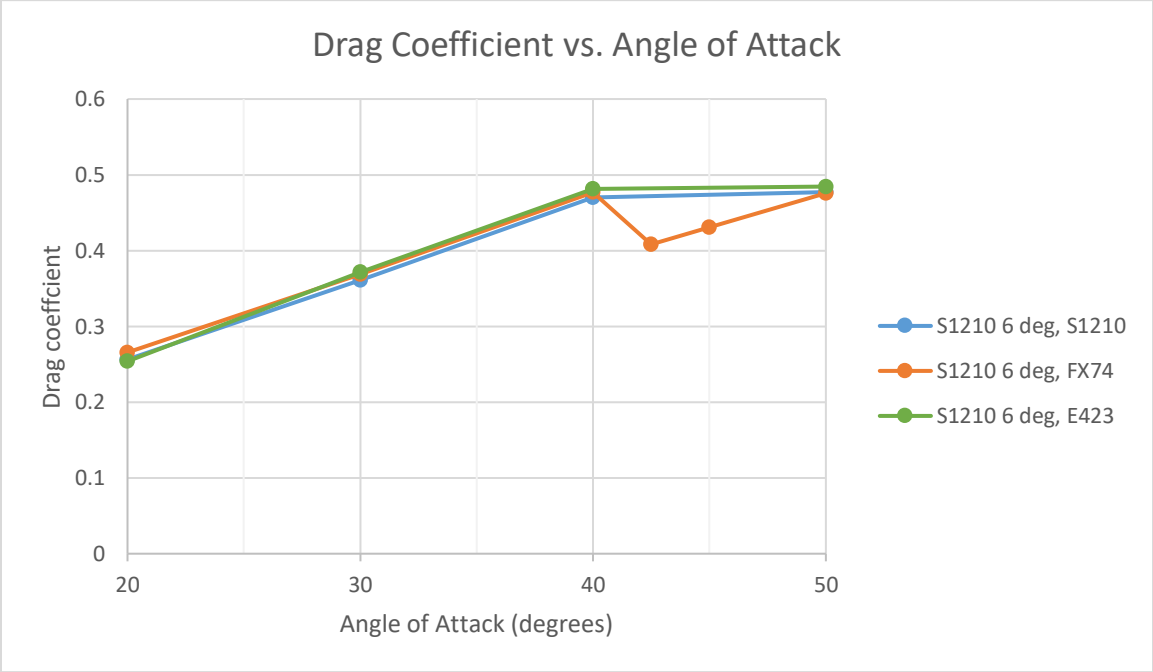

Figure 18 Computed drag coefficient of two-element airfoils at various flap α

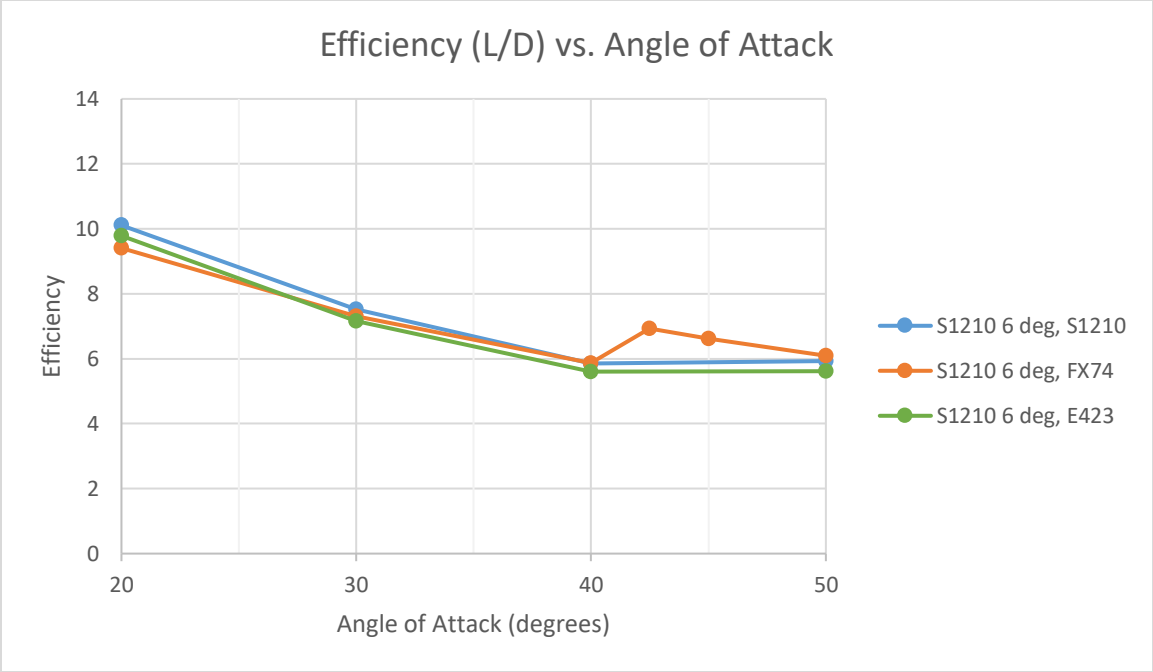

Figure 19 Computed L/D of two-element airfoils at various flap α

It is important to note from these figures that the negative lift keeps increasing with increase in flap α from 20º to 50º. It should be noted that a 50 degree flap angle is the upper limit for this specific configuration since it corresponds to the maximum allotted height from the FSAE Rules. At lower angles of attack, the S1210 flap is superior to the FX74 flap but the negative lift values cross between 30 and 40 degrees. Since the angle is so large, the airfoil is further away from the ground, and as shown in Figure 13, the FX74 airfoil has a higher negative lift coefficient than the S1210 at higher values of h, therefore this could be a reason for its superior performance. Figure 20 shows the velocity contours of the S1210 main element and FX74 flap, two-element airfoil at flap α of 20º and 50º (before and after separation).

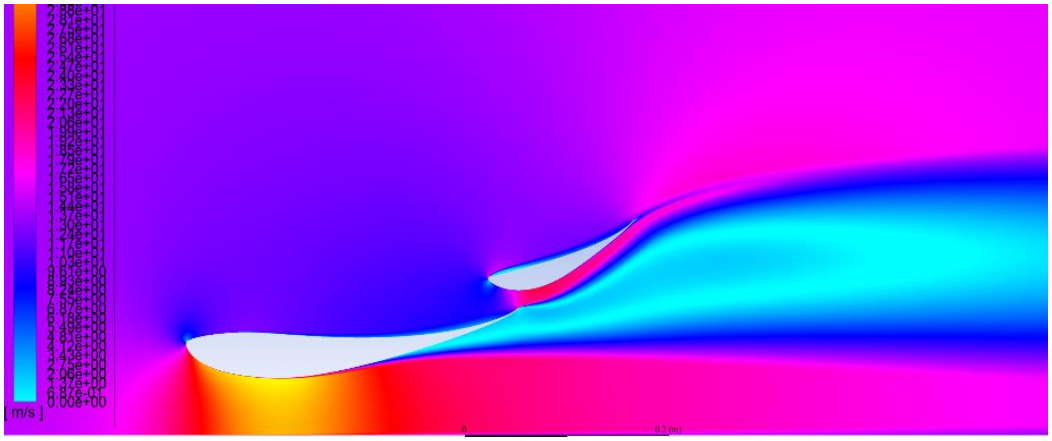

(a) α_{flap} = 20º

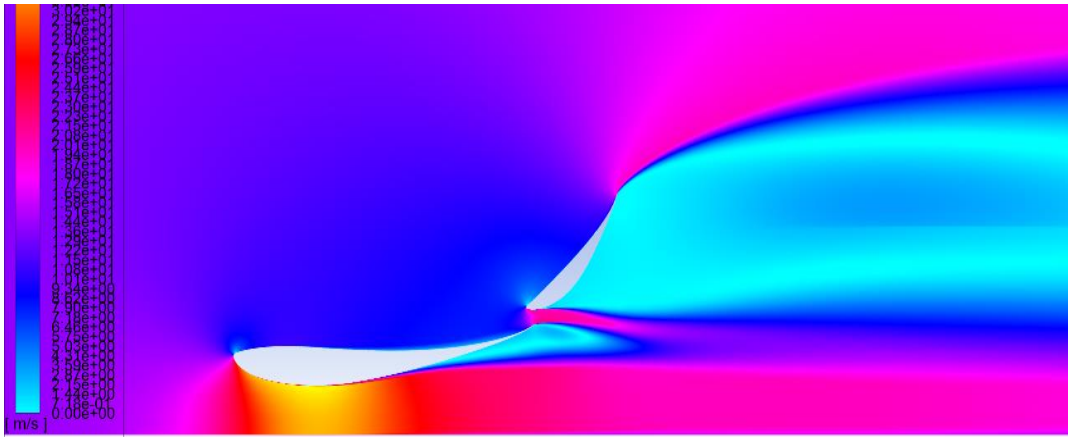

(b) α_{flap} = 45º

Figure 20 Velocity contours for S1210 main element at α = 6º with FX74 flap in ground effect

It is worth noting that the flow separates from the flap at flap α between 40º and 42.5º; this is the reason for sudden change in negative lift, drag, and efficiency in Figures 17-19. It was of interest to determine if the flow separation occurred due to ground effect or due to some other reason; therefore two identical cases at 40º and 45º were run without any ground effect. Figure 21 shows the results in the form of velocity contours. It is evident that the flow has already separated before the flap angle reaches 40º; the ground effect in Figure 20 delays the flow separation from the flap and therefore allows for a larger lift generation than would be possible at the same angles of attack further away from the ground.

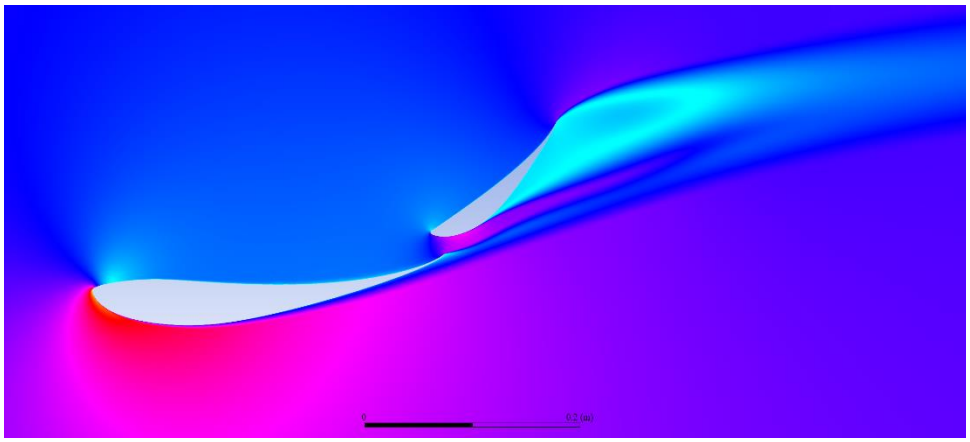

(a) $\alpha_{flap} = 40^o$

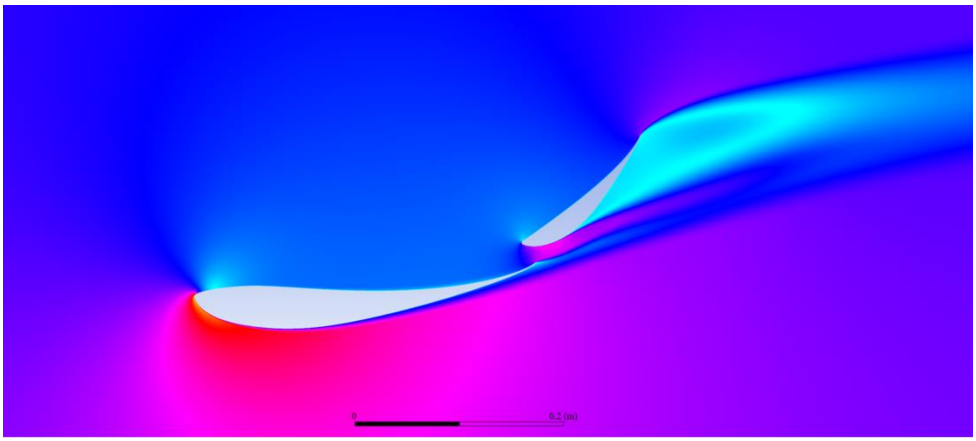

(b) $\alpha_{flap} = 45^o$

Figure 21 Velocity contours for S1210 main element at $\alpha = 6^o$ and FX74 flap without ground effect

4.2 Main Element Airfoil and Flap Angles of Attack

It was determined in Section 4.1 that the FX74 flap was superior at higher flap angles of attack; therefore it was selected as the flap of choice in the following studies. The h was maintained at 0.0508 m and the c for the main element and flap were kept constant. Also, vertical and horizontal spacing between the main element and flap were set at a constant value. Main element angles of attack were changed from -6 to 9 degrees in increments of 3 degrees, and for each main element α, flap angles were varied from 20 to 50 degrees in increments of 10 degrees. The results for negative lift coefficient, drag coefficient, and efficiency are shown in Figures 22-24. Legends in the figures, e.g. "Main 9 degrees" implies that the main element S1210 airfoil is set with $\alpha = 9^{o}$.

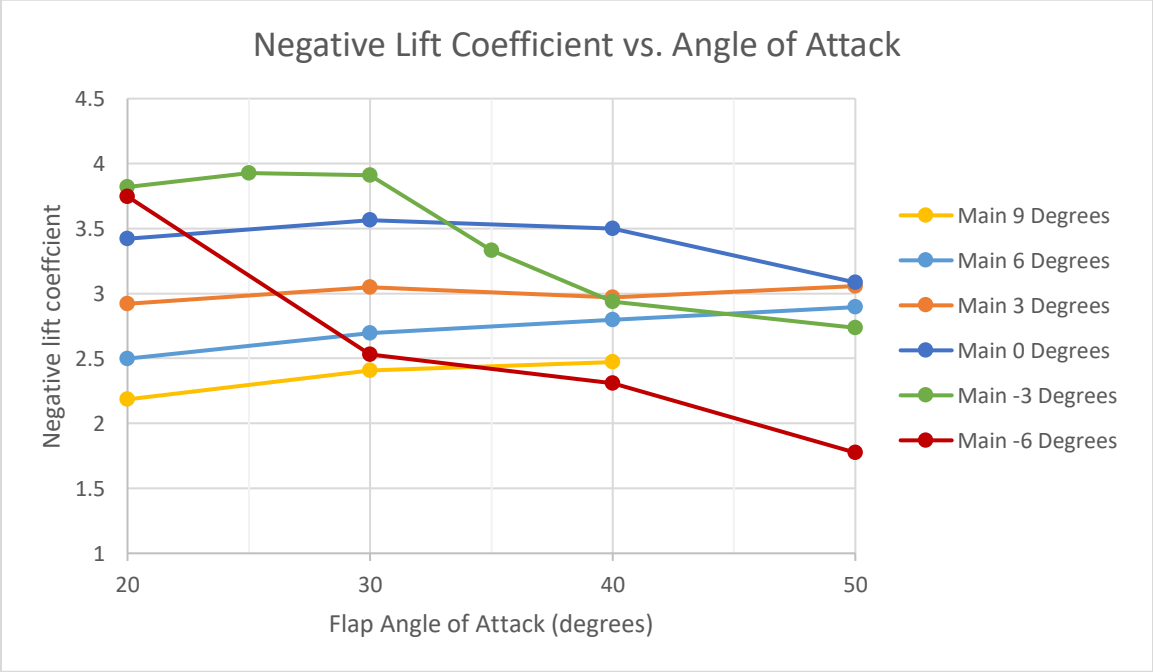

Figure 22 Negative lift coefficients for various flap (FX74) α with main element (S1210) at different α

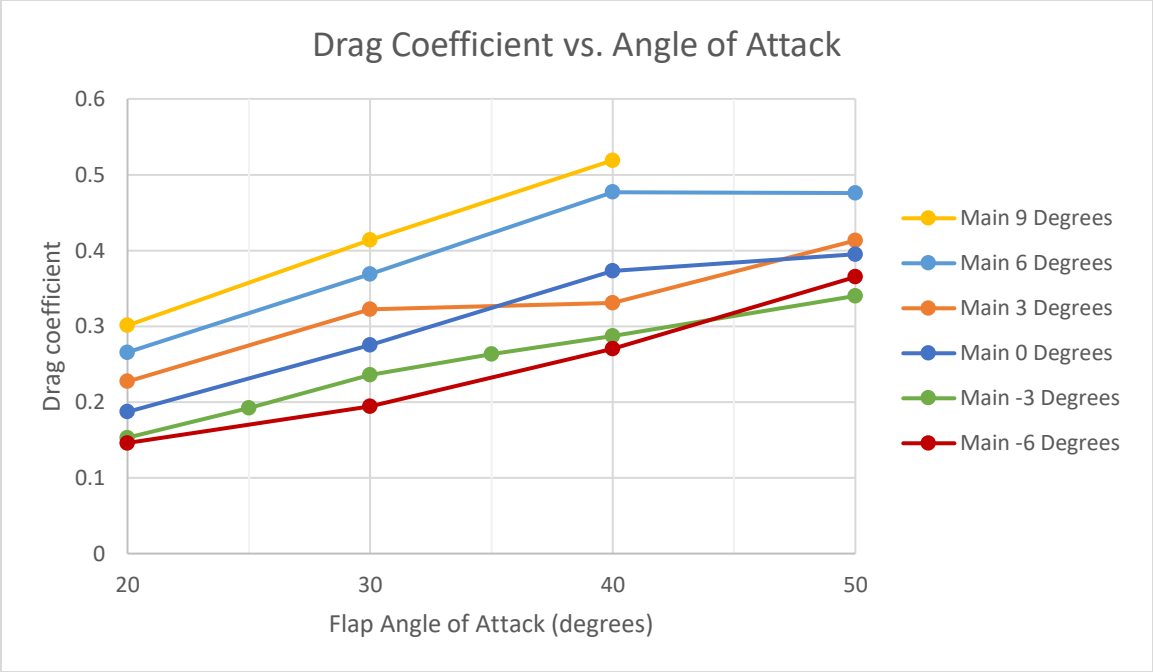

Figure 23 Drag coefficients for various flap (FX74) α with main element (S1210) at different α

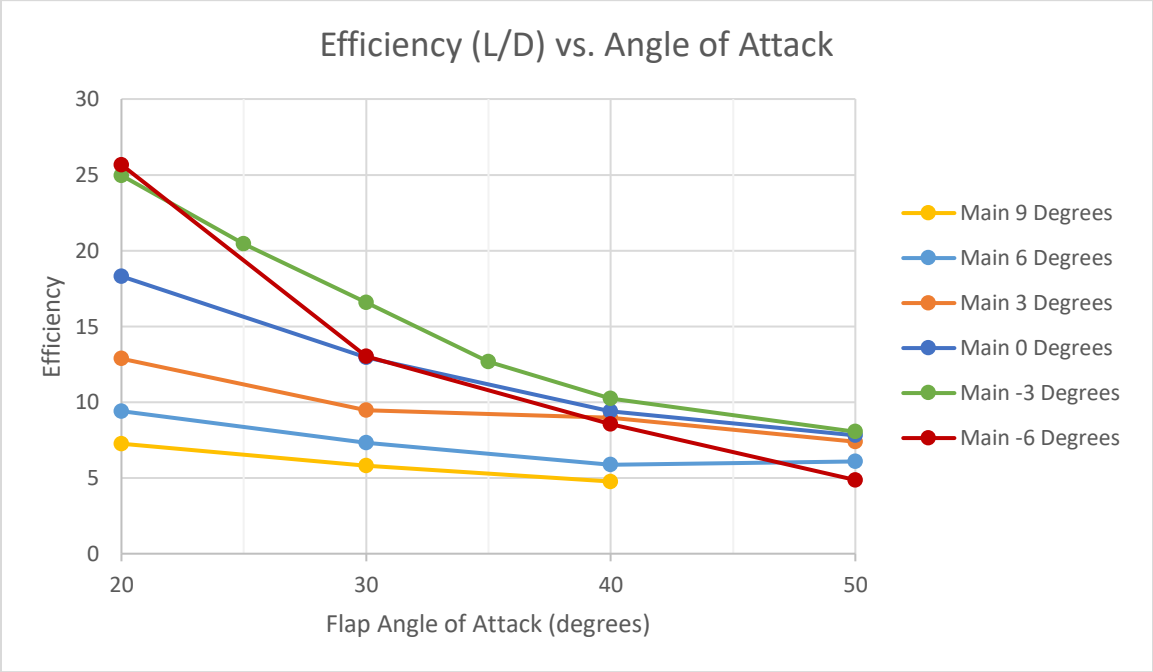

Figure 24 Efficiency for various flap (FX74) α with main element (S1210) at different α

Literature indicates that the addition of a flap delays flow separation and allows for greater main element α; therefore main element α of 6 and 9 degrees were initially considered. It was found that the main element at $\alpha = 9^o$ had less negative lift than at $\alpha = 6^o$; consequently subsequent runs for main element α of less than 6^o all the way down to -6^o performed, at which the negative lift coefficient no longer increased. This is a surprising result since the single element airfoil negative lift increases between α = 0 to 9 degrees. It is clear from Figure 22 that at higher main element α, the flap can continue to generate more downforce with increase in α, but the magnitude of negative lift generated by the flap is much smaller than that from the main element $\alpha = 0^o$ or less (negative angles). At lower main element α, this trend continues until the flow separates – once the flow separates the lift generation significantly drops. A comparison of velocity contours around a pre-flow separation airfoil and a post-flow separation airfoil is shown in Figures 25 and 26.

As shown in Figure 23, drag coefficient steadily increases as flap α increases, and the drag coefficient decreases with a decrease in α of the main element. The negative α of the main element is therefore very beneficial from an efficiency view as can be seen from Figure 24, the main element at $\alpha = -3^o$ is the most efficient α and generates the most downforce.

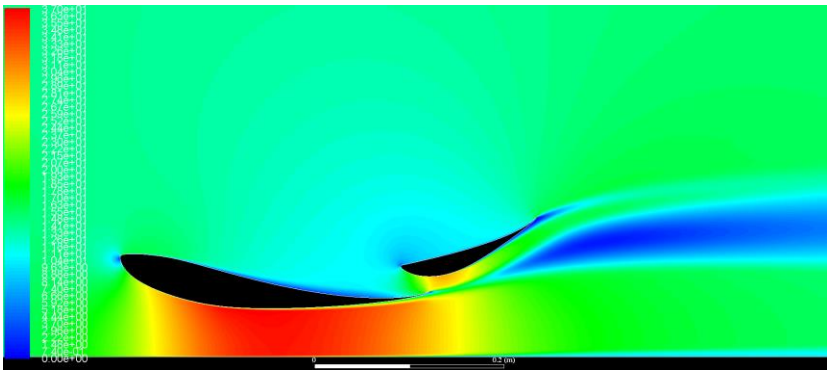

(a) $\alpha_{main} = -6^o$, $\alpha_{flap} = 20^o$

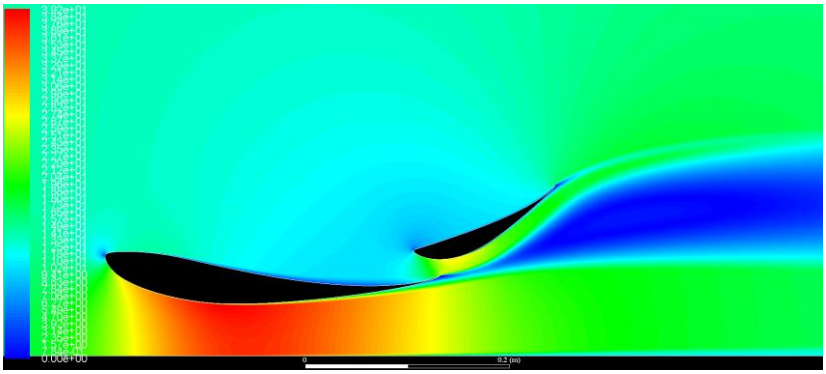

(b) $\alpha_{main} = -3^o$, $\alpha_{flap} = 25^o$

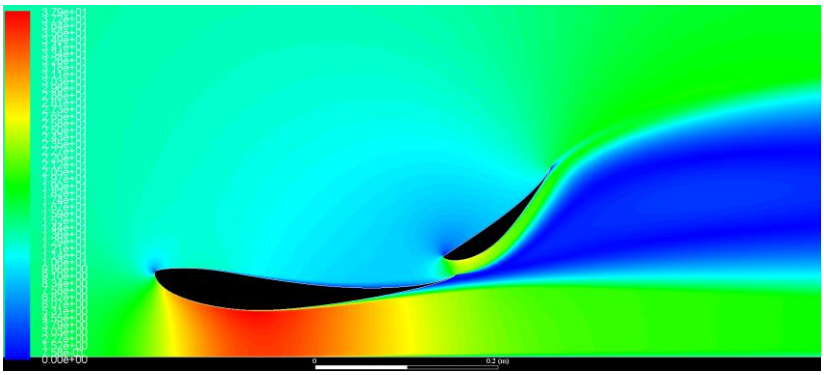

(c) $\alpha_{main} = 0^o$, $\alpha_{flap} = 40^o$

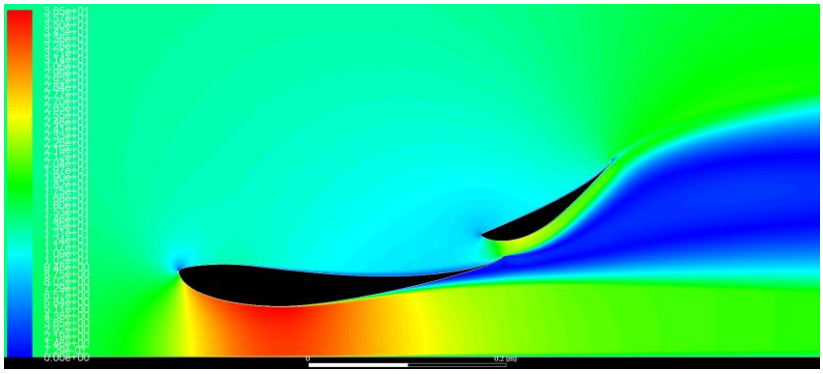

(d) $\alpha_{main} = 3^o$, $\alpha_{flap} = 40^o$

Figure 25 Velocity contours for various main element (S1210) α and flap (FX74) α before flow separation

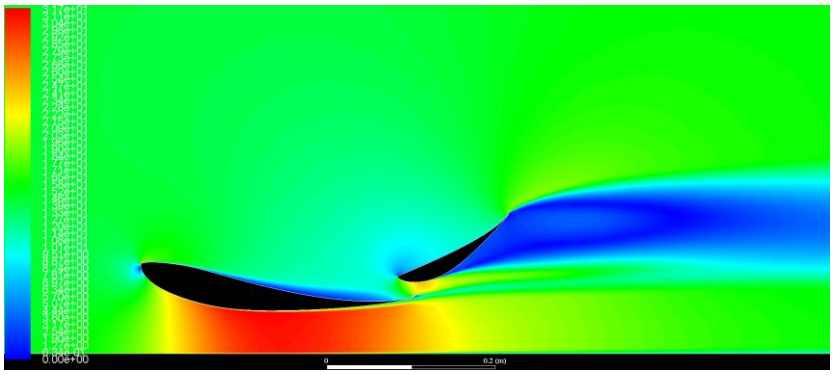

(a) $\alpha_{main} = -6^o$, $\alpha_{flap} = 30^o$

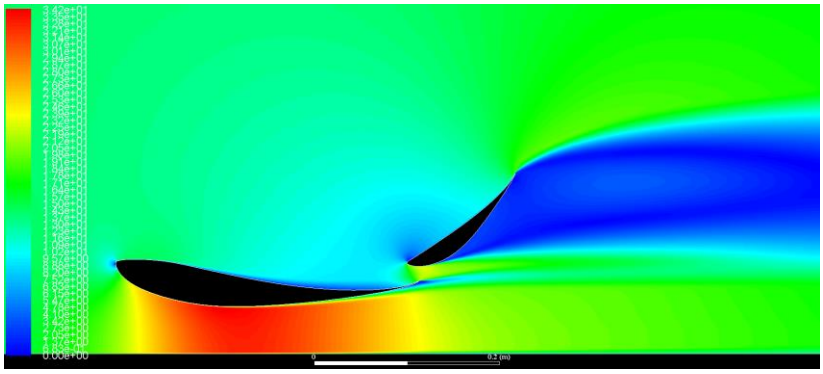

(b) $\alpha_{main} = -3^o$, $\alpha_{flap} = 40^o$

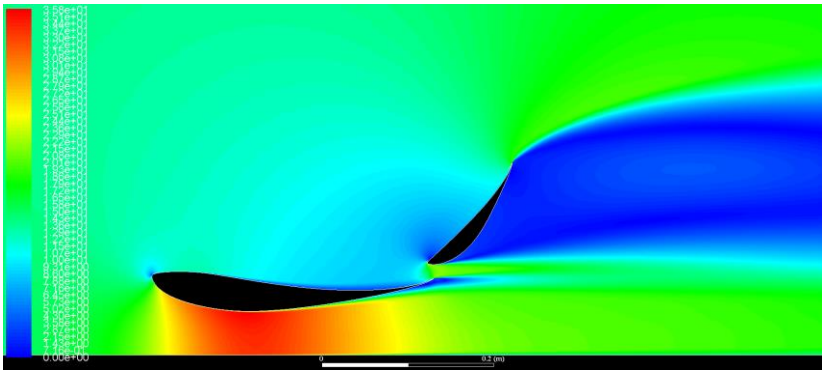

(c) $\alpha_{main} = 0^o$, $\alpha_{flap} = 50^o$

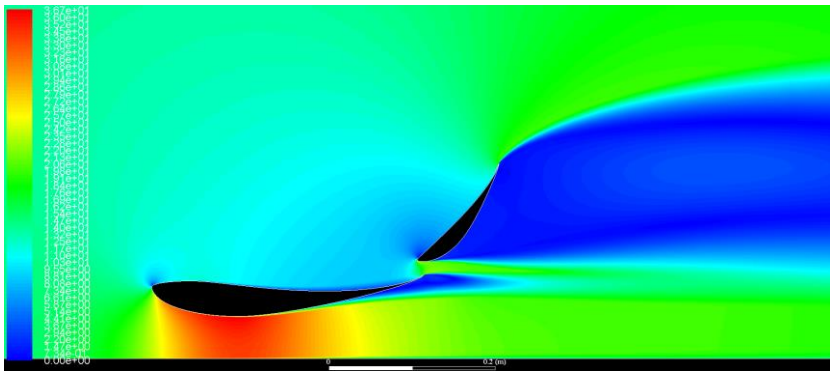

(d) $\alpha_{main} = 3^o$, $\alpha_{flap} = 50^o$

Figure 26 Velocity contours for various main element (S1210) α and flap (FX74) α after flow separation

The velocity contour plots (a)-(d) in Figures 25 and 26 show comparisons of the flow fields of two-element airfoils before and after flow separation at various α of the main element and flap airfoils. At main element α = -6^o and -3^o, the wake is nearly detached from the trailing edge of the main element. The attached flow of the flap causes this nearly detached wake and evidently it is beneficial for lift generation and drag reduction. When the α of the flap is set too high, causing flow separation from the flap, the detached wake is completely eliminated, hence the significant decrease in negative lift coefficient can be seen. The detached wake does not occur for main element at α = 0^o or higher; the main element has a very small region of flow separation from the trailing edge that leads into an attached wake at lower flap angles. Once the flow separates from the flap, the same condition occurs as for the main element at smaller α; the wake region is eliminated, and the negative lift continues to grow at higher main element α, shown in Figure 17.

4.3 Main Element Airfoil and Flap Height Above the Ground

Based on the study in Section 4.2, a combination of the main element airfoil (S1210) α = -3^o and the flap (FX74) α = 25^o are considered for the study of ground effect by varying the two-element airfoil h. Figure 27 defines the location for describing the ground height which is varied from 0.0381 m to 0.1016 m; this height is designated as “H1”. Figures 28 - 30 show the negative lift coefficient, drag coefficient, and the efficiency as the ground height changes.

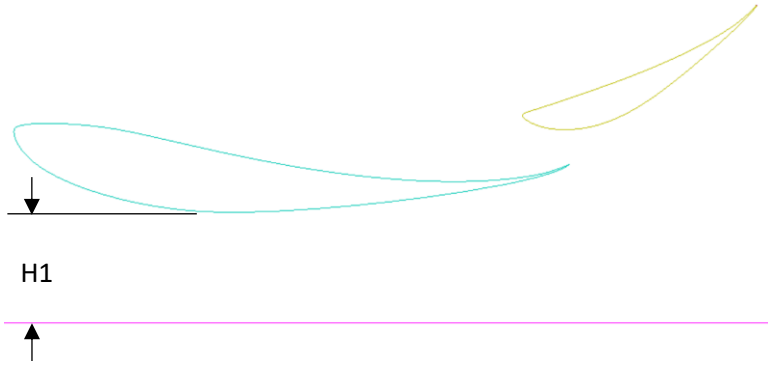

Figure 27 Definition of height above the ground, H1

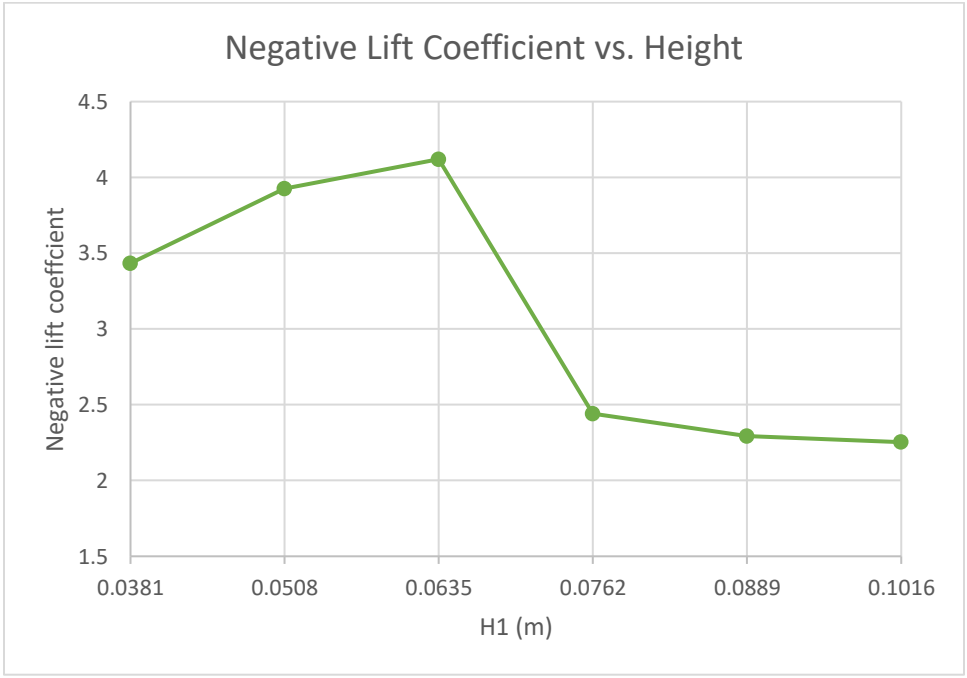

Figure 28 Negative lift coefficient for various H1 for a two-element airfoil with S1210 (main element) at α = -3º and FX74 (flap) at α = 25º

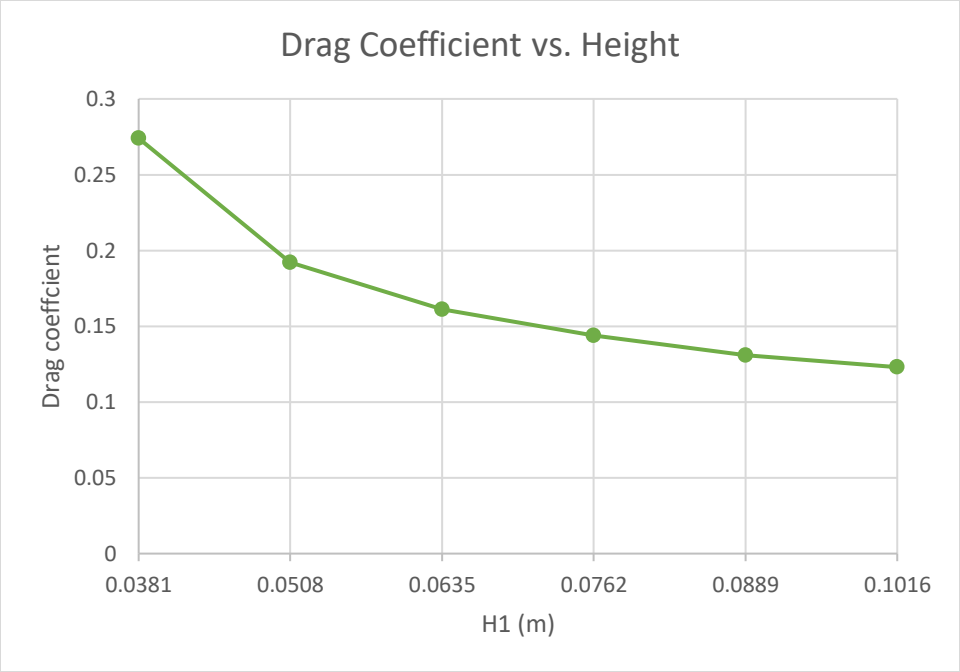

Figure 29 Drag coefficient for various H1 for a two-element airfoil with S1210 (main element) at α = -3º and FX74 (flap) at α = 25º

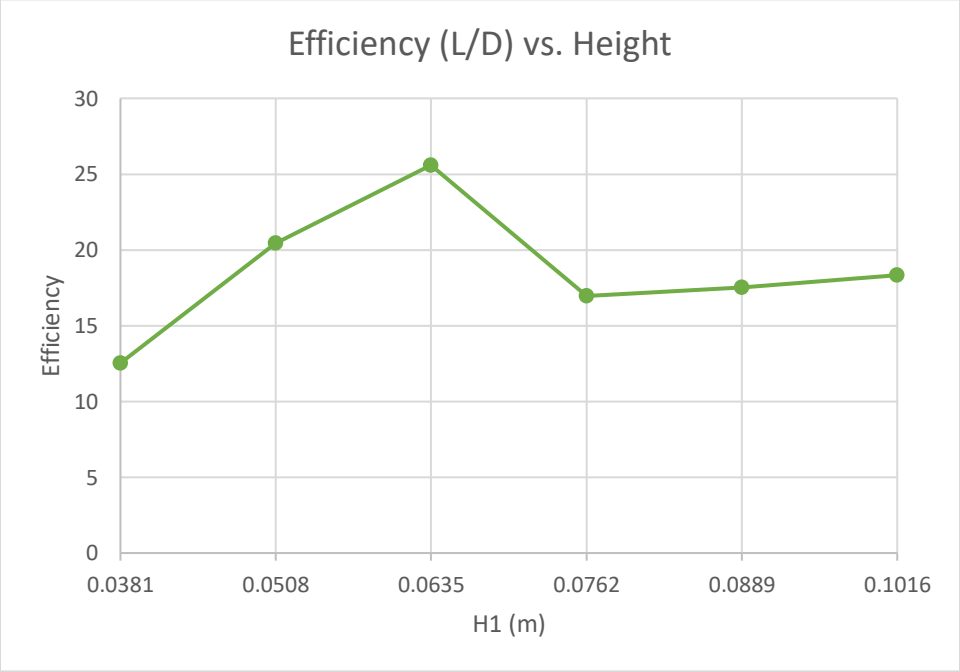

Figure 30 Efficiency for various H1 for a two-element airfoil with S1210 (main element) at α = -3º and FX74 (flap) at α = 25º

From Figures 28-30, an optimal H1 = 0.0635 m was determined with $-C_L = 4.120$. Although it is an ideal choice for ground height, in the following studies H1 = 0.0508 m was selected due to packaging requirements of the WashU Racing Formula SAE car. There is limited room under the nosecone of the race car, therefore a lower height became necessary to fit the two-element wing on the car. The $-C_L = 3.927$ for H1 = 0.0508 m, an approximate loss of a $-C_L = 0.20$ m, but it is necessary for fitment purposes. There is a significant drop in negative lift coefficient between the heights of 0.0635 m and 0.0762 m, which was not the trend found for the single element airfoils in Chapter 3. At the lowest height, H1 = 0.0381 m, there is an attached wake to the trailing edge of the main element which detaches itself as H1 increases from 0.0508 m to 0.0635 m. Once the height reaches 0.0762 m the flow separates from the flap, causing a dramatic decrease in negative lift generation. Figure 31 shows the velocity contours for various H1 for the two-element configuration.

The large changes in negative lift can possibly be attributed to the interaction of the boundary layer on the main element with the ground boundary layer. At heights that are too close to the ground, there may be increased amounts of boundary layer interference between the ground and the main element not allowing for enough vertical space for the air to accelerate. This is evident in Figure 28 where the negative lift coefficient at H1 = 0.0381 m is lower than that at H1 = 0.0508 m and 0.0635 m. The drag is also higher at lower H1 values from the boundary layer interference; the drag coefficient decreases rapidly when H1 increases ($R^2 = 0.973$). However from an efficiency perspective, the heights for the maximum negative lift generation H1 = 0.0508 m and 0.0635 m are the most efficient points; therefore both of these heights are a good choice for the two-element configuration.

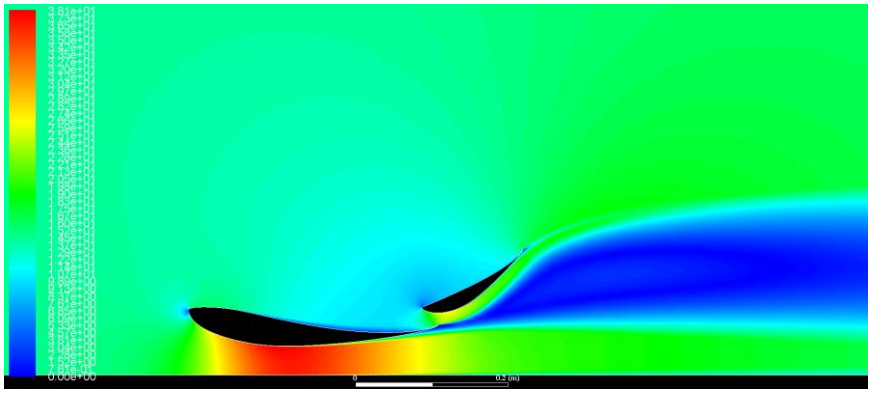

(a) H1 = 0.0381 m

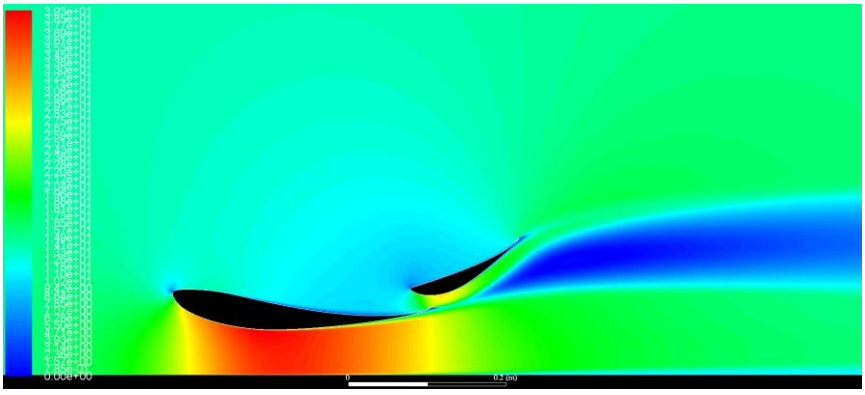

(b) H1 = 0.0508 m

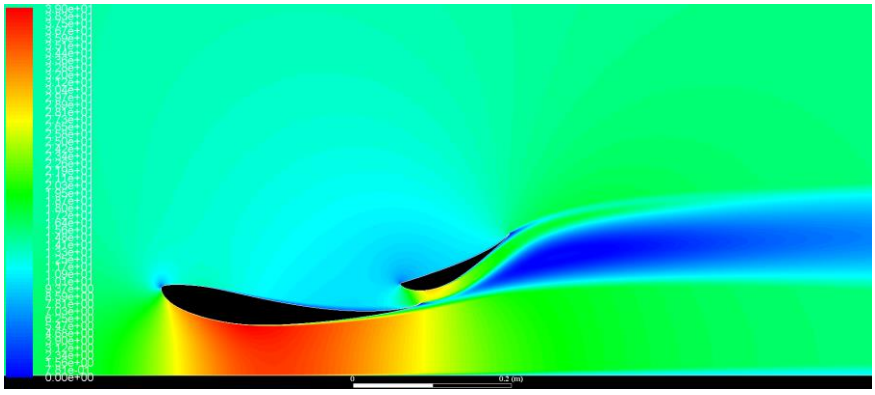

(c) H1 = 0.0635 m

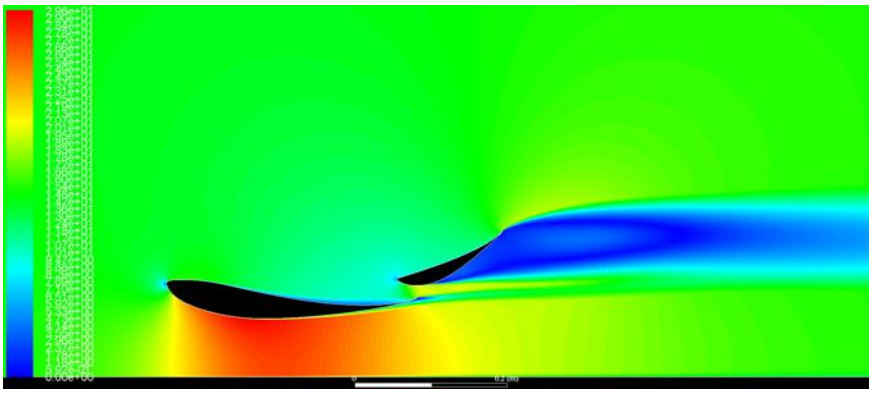

(d) H1 = 0.0762 m

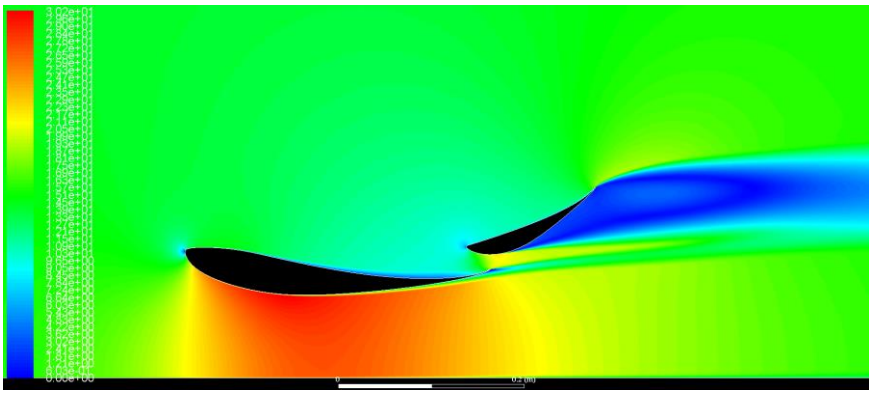

(e) H1 = 0.0889 m

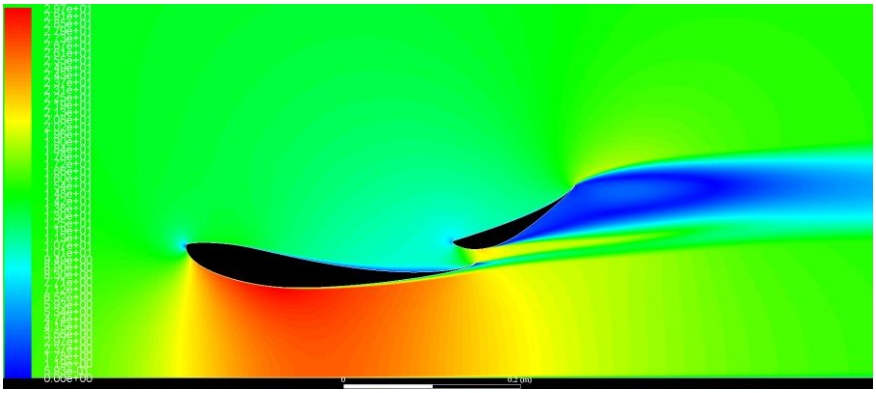

(f) H1 = 0.1016 m

Figure 31 Velocity contours for various H1 for the selected two-element configuration

4.4 Flap Vertical Spacing

With the optimal two element airfoil combination being selected as the S1210 main element at $\alpha = -3^o$ and the FX74 flap at $\alpha = 25^o$, with the two-element ground height H1 = 0.0635 m, the next optimization step is to study the effect of vertical spacing of the flap above the main element. This spacing of the flap is designated as "H2" and is calculated from the lowest point on the flap to the tip of the trailing edge of the main element as shown in Figure 32. The height of the gap between the main element and flap influences the airflow passing between them and affects the circulation on the main element. This study was conducted on two, two-element airfoil configurations. The vertical spacing, H2, was varied from H2 = 0.012 m to 0.028 m in increments of 0.002 m for main element $\alpha = -3^o$, with flap at $\alpha = 25^o$. In the second case H2 was varied from 0.008 m to 0.018 m in increments of 0.002 m for the main element $\alpha = 6^o$, with flap $\alpha = 50^o$. Negative lift coefficient, drag coefficient, and efficiency are shown in Figures 33-35. Figure 36 shows velocity contours pre and post flow separation. An optimal H2 value was found as H2 = 0.020 m with a $-C_L = 4.223$. The legend in these figures, e.g. "Main -3 Degrees, Flap 25 Degrees" implies that the main element is the S1210 airfoil with $\alpha = -3^o$ and the flap is the FX74 airfoil with $\alpha = 25^o$.

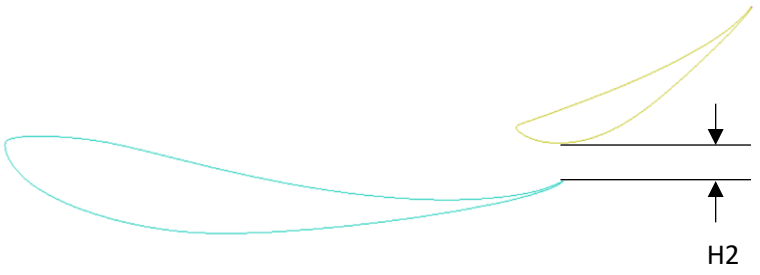

Figure 32 Definition of flap vertical spacing, H2

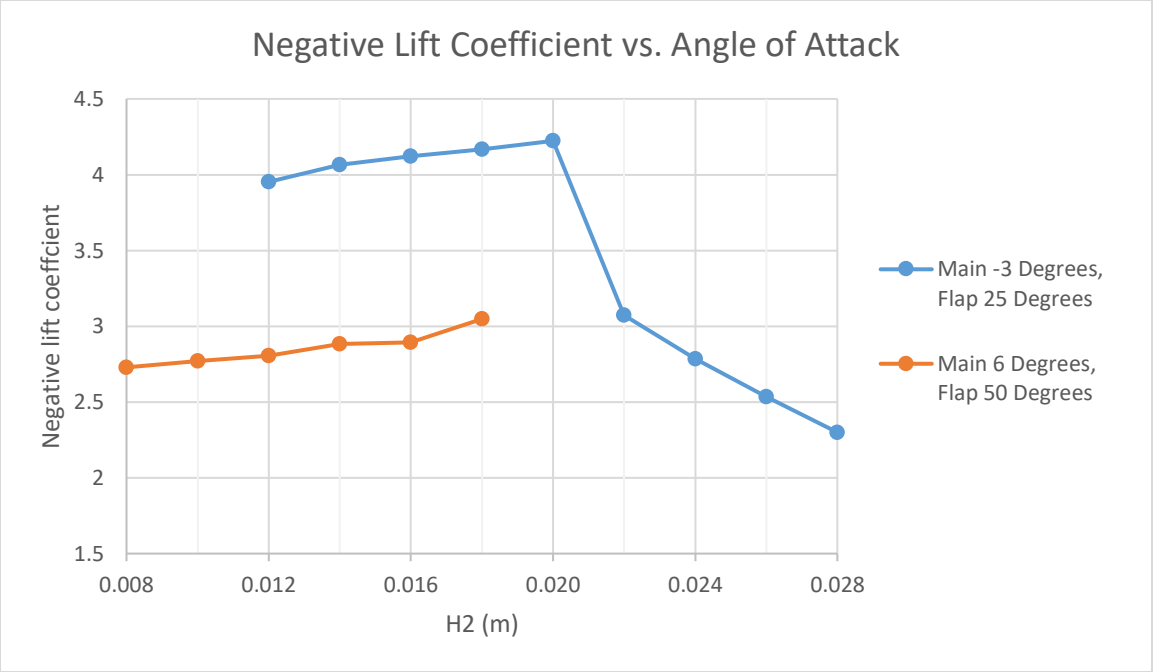

Figure 33 Negative lift coefficients for various H2 for two cases

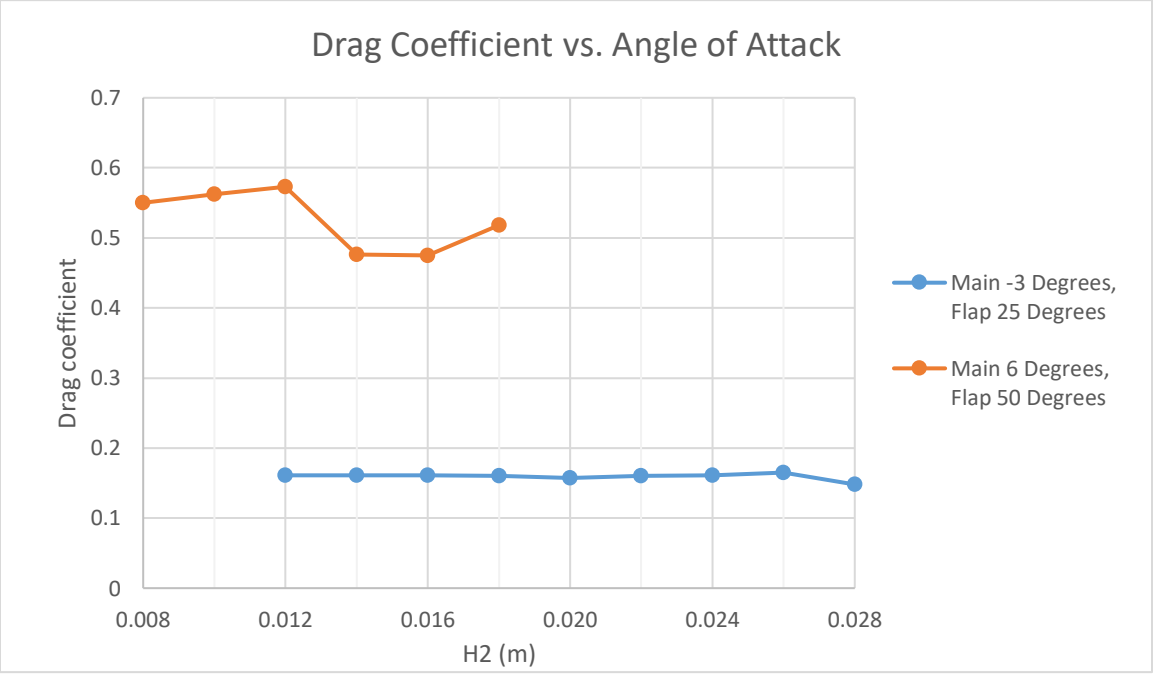

Figure 34 Drag coefficients for various H2 for two cases

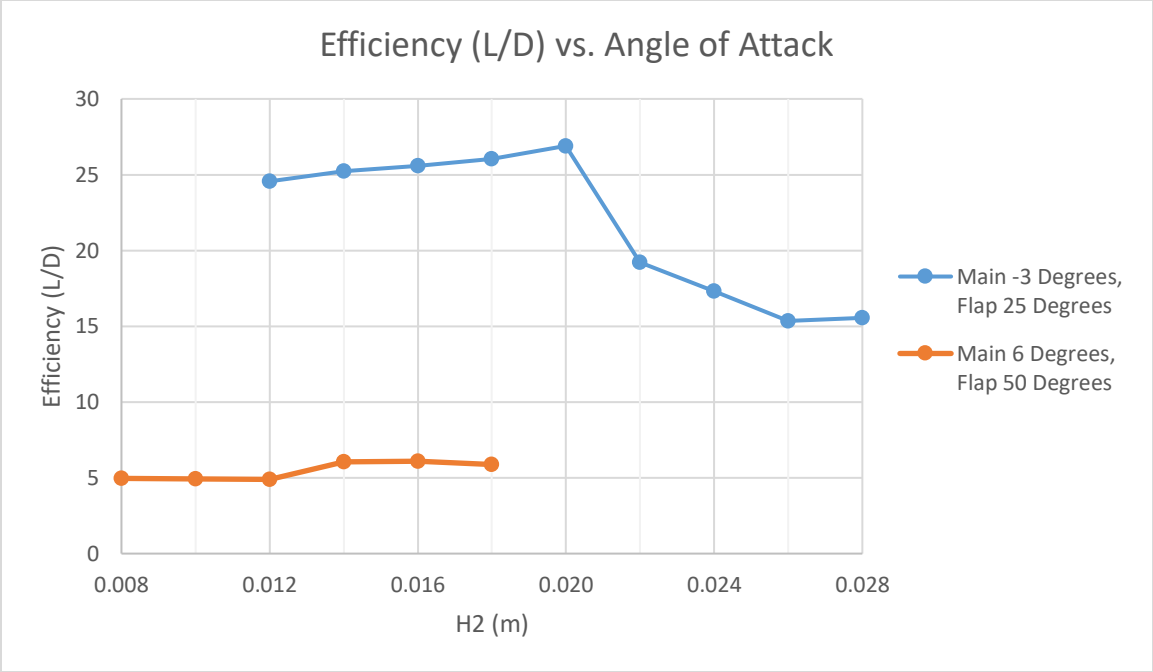

Figure 35 Efficiency for various H2

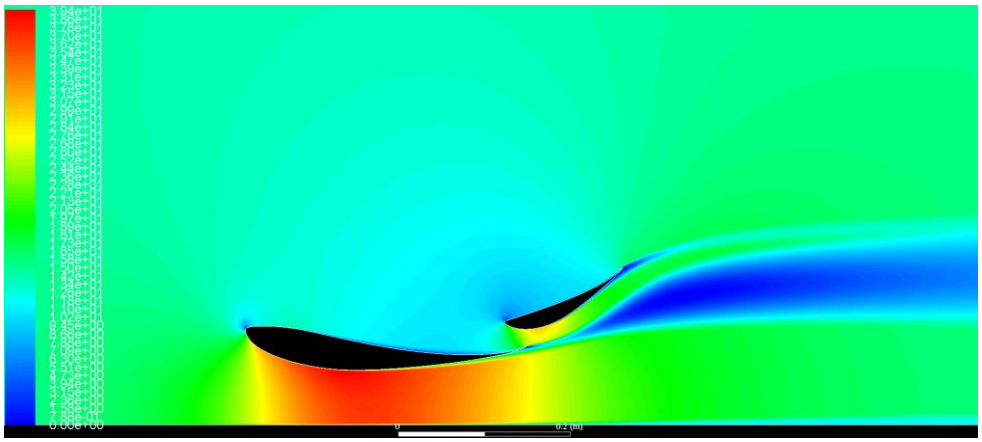

(a) H2 = 0.020 m, pre-separation, α_{main} = -3°, α_{flap} = 25°

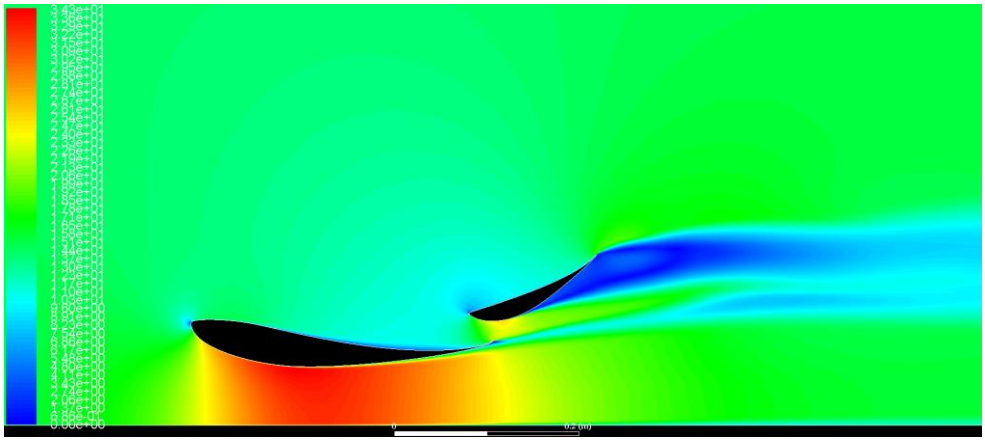

(b) H2 = 0.022 m, post-separation, α_{main} = -3°, α_{flap} = 25°

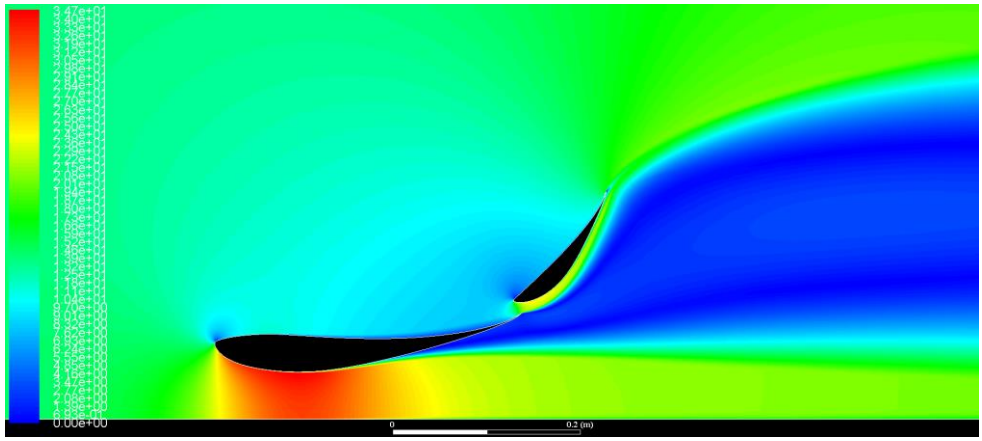

(c) H2 = 0.012 m, pre-separation, α_{main} = 6°, α_{flap} = 50°

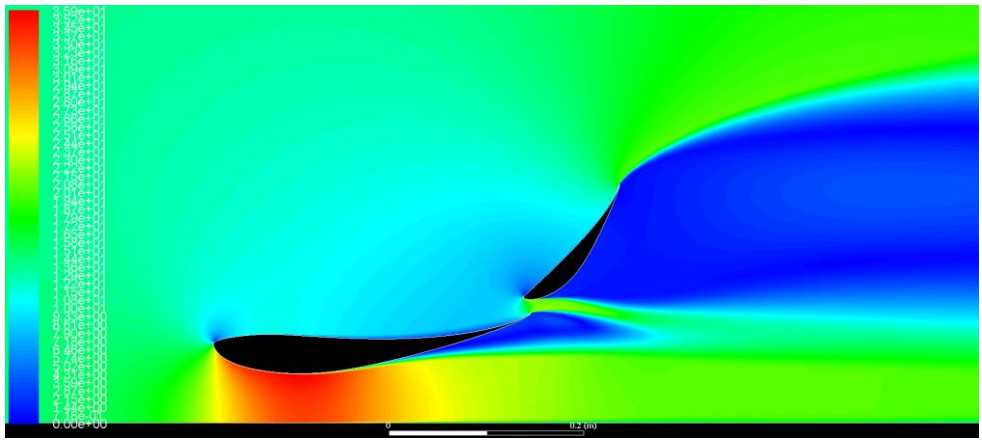

(d) H2 = 0.014 m, post-separation, α_{main} = 6°, α_{flap} = 50°

Figure 36 Velocity contours for various H2

4.5 Flap Horizontal Spacing

Again, the optimal two element airfoil combination was selected as the S1210 main element at $\alpha = -3^o$ and the FX74 flap at $\alpha = 25^o$, with the two-element ground height H1 = 0.0635 m, and the flap vertical spacing H2 = 0.020 m. The final optimization step in this thesis is to study the effect of horizontal spacing of the flap fore/aft of the trailing edge of the main element. This flap spacing is designated as "H3" and is defined from the leading edge of the flap to the tip of the trailing edge of the main element as shown in Figure 37. Again, this study was conducted on two, two-element airfoil configurations, same as in Section 4.4. The horizontal spacing, H3, is varied from -0.037 m to -0.013 m in increments of 0.002 m for the first case of the main element at $\alpha = -3^o$, with flap at $\alpha = 25^o$. In the second case H3 was varied from -0.024 m to 0.000 m in increments of 0.004 m for the main element $\alpha = 6^o$, with flap $\alpha = 50^o$. Negative lift coefficient, drag coefficient, and efficiency are shown in Figures 38-40. Figure 41 shows the velocity contours pre and post flow separation. An optimal H3 value was found as H3 = -0.023 m with a $-C_L = 4.263$. The legend in these figures, e.g. "Main -3 Degrees, Flap 25 Degrees" implies that the main element is the S1210 airfoil with $\alpha = -3^o$ and the flap is the FX74 airfoil with $\alpha = 25^o$.

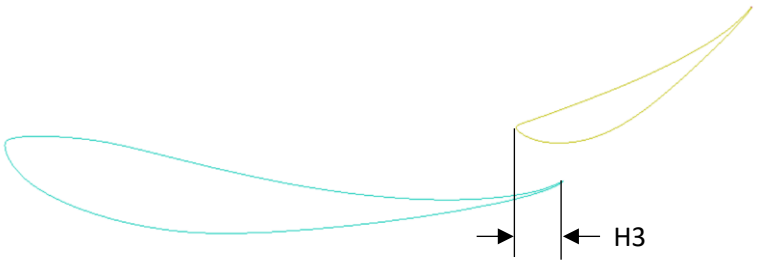

Figure 37 Definition of flap horizontal spacing, H3

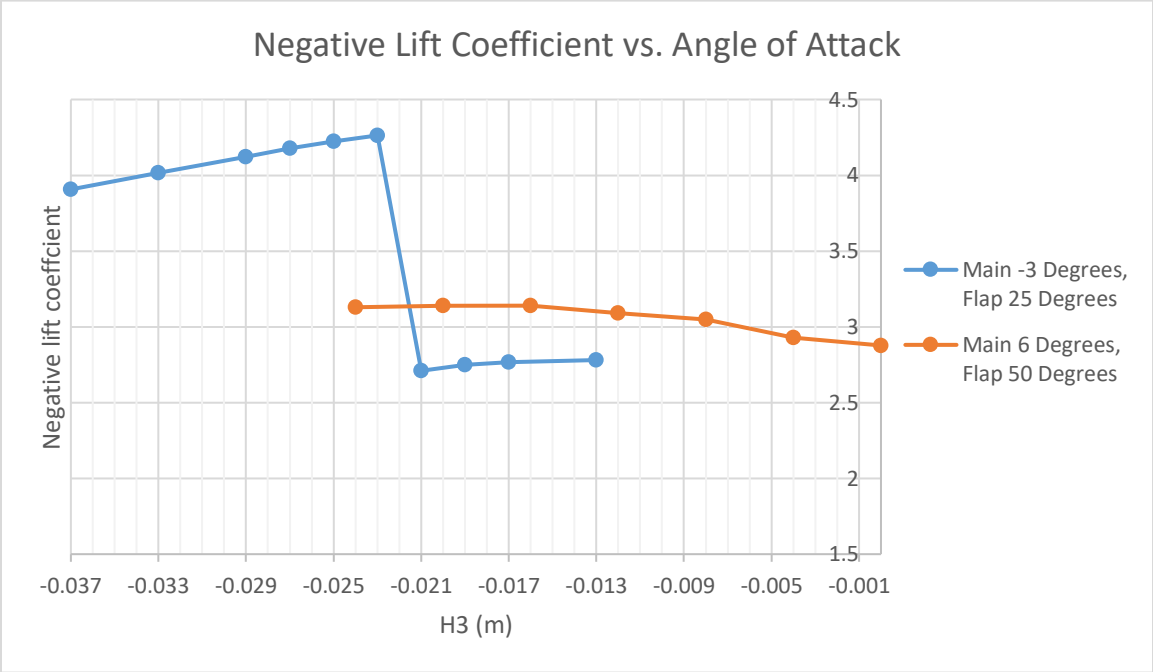

Figure 38 Negative lift coefficients for various H3 for two cases

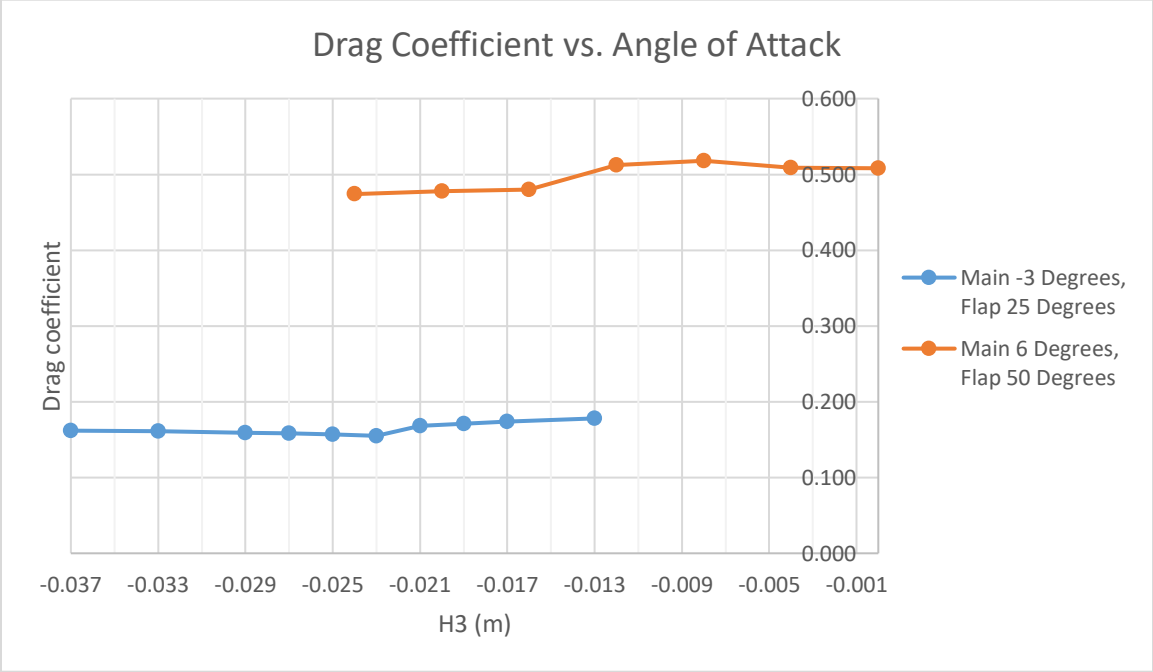

Figure 39 Drag coefficients for various H3 for two cases

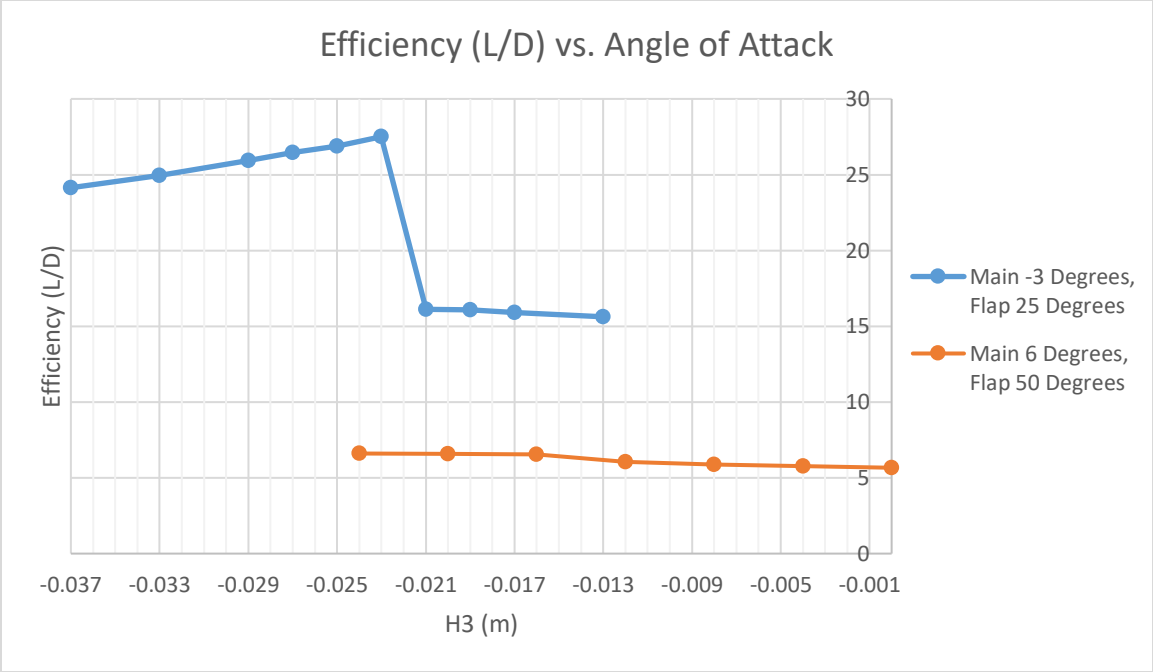

Figure 40 Efficiency for various H3 for two cases

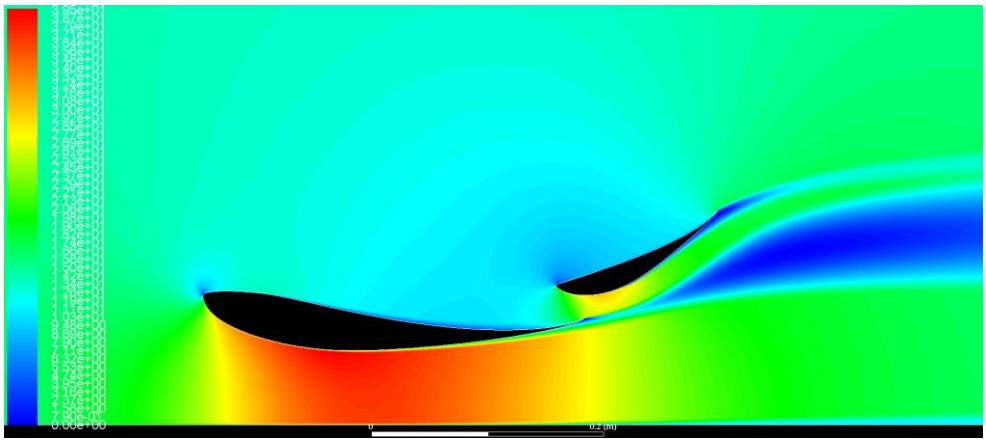

(a) H3 = -0.023 m, pre-separation, α_{main} = -3°, α_{flap} = 25°

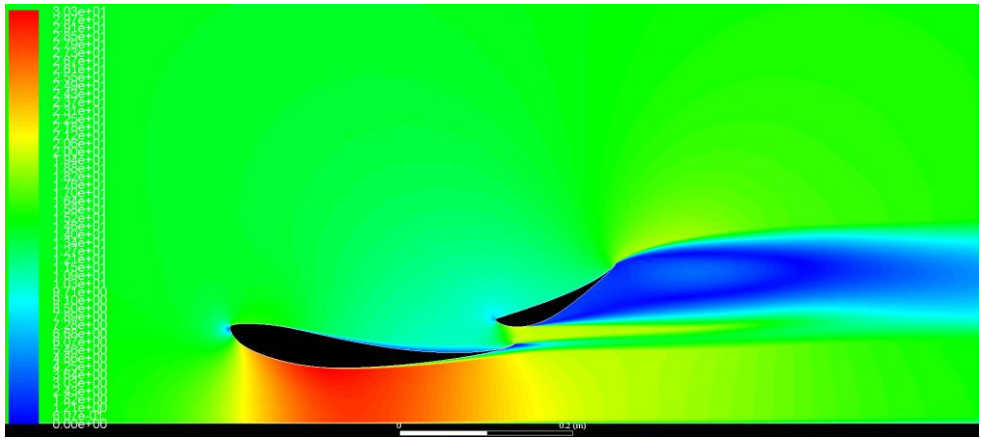

(b) H3 = -0.021 m, post-separation, α_{main} = -3º, α_{flap} = 25º

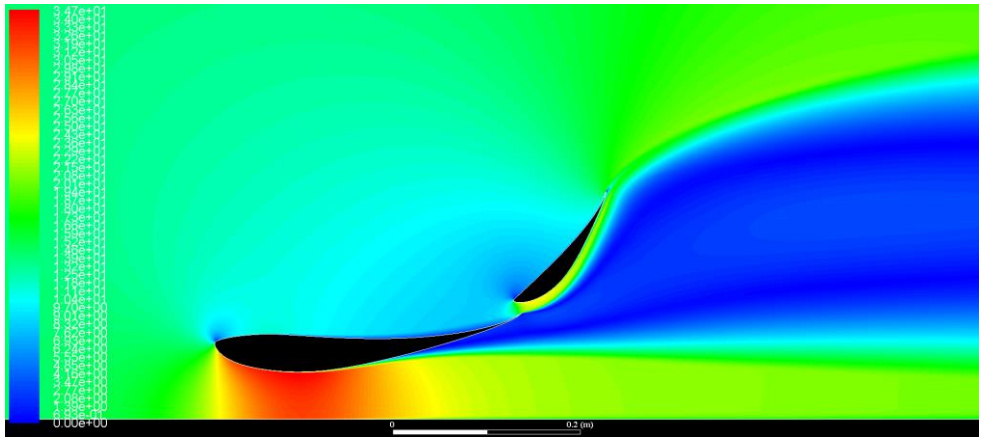

(c) H3 = -0.008 m, pre-separation, α_{main} = 6º, α_{flap} = 50º

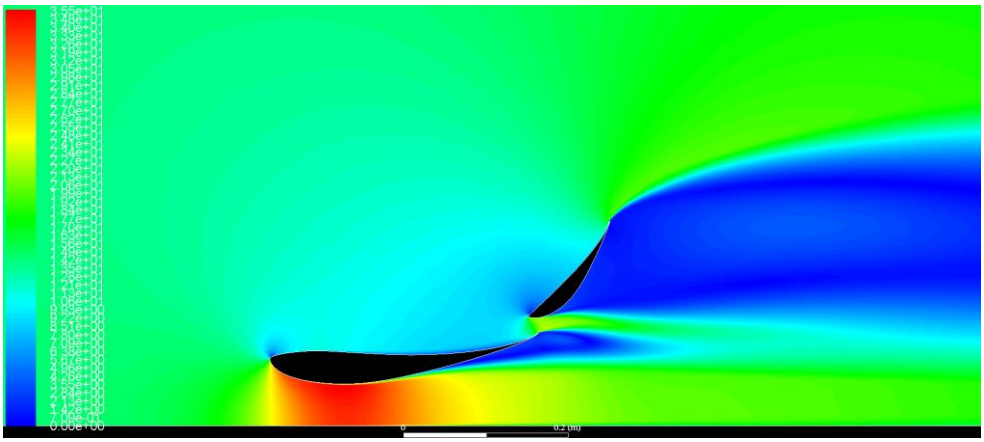

(d) H3 = -0.012 m, post-separation, α_{main} = 6º, α_{flap} = 50º

Figure 41 Velocity contours for various H3

4.6 Final Selected Configuration of Multi-Element Airfoil

Based on the results presented in the previous sections, the specification of the optimal two-element airfoil configuration for an FSAE race car is as follows: an S1210 main element with c = 0.33 m at $\alpha = -3^o$, FX74 flap with c = 0.1524 m at $\alpha = 25^o$; ground height H1 = 0.0508 m, flap vertical spacing H2 = 0.020 m, and flap horizontal spacing H3 = -0.023 m. This configuration generates $-C_L = 4.263$, $C_D = 0.155$, L/D = 27.50. To examine how much the effect the close proximity to the ground has on this two-element configuration, one can examine Figures 42 and 43. A study with the identical configuration was conducted except H1 was changed to 1.000 m to remove any ground effect. This ground height generated $-C_L = 1.538$, $C_D = 0.067$, L/D = 22.96. Thus, the ground effect with H1 = 0.0508 m is very significant; the negative lift coefficient of the optimized configuration was nearly 2.78x greater than the configuration without ground effect.

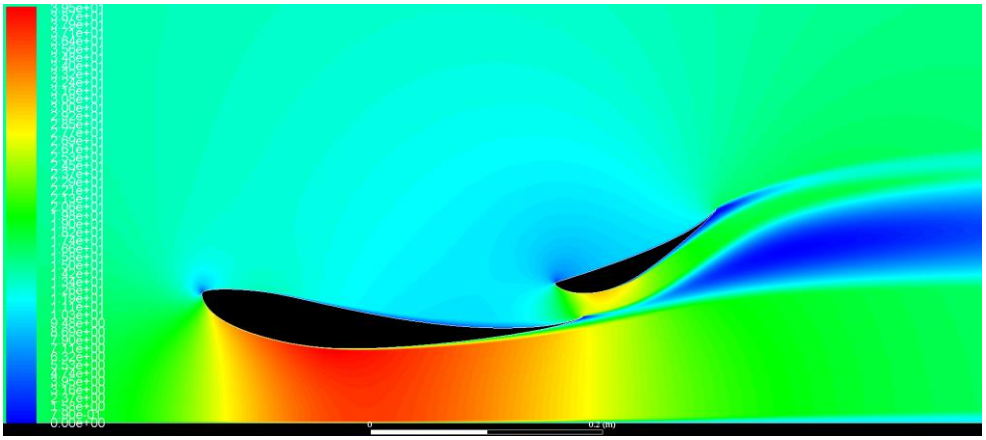

(a) Optimized configuration in ground effect

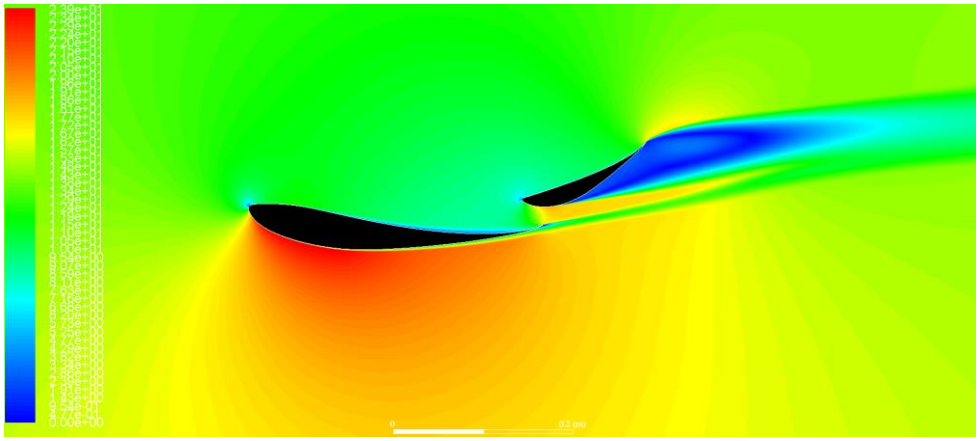

(b) Optimized configuration without ground effect

Figure 42 Velocity contours of the optimized configuration with and without ground effect

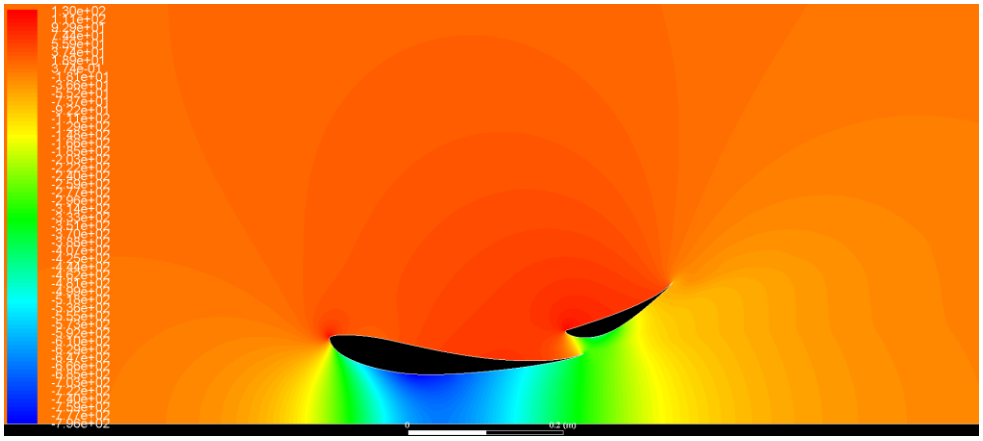

(a) Optimized configuration with ground effect

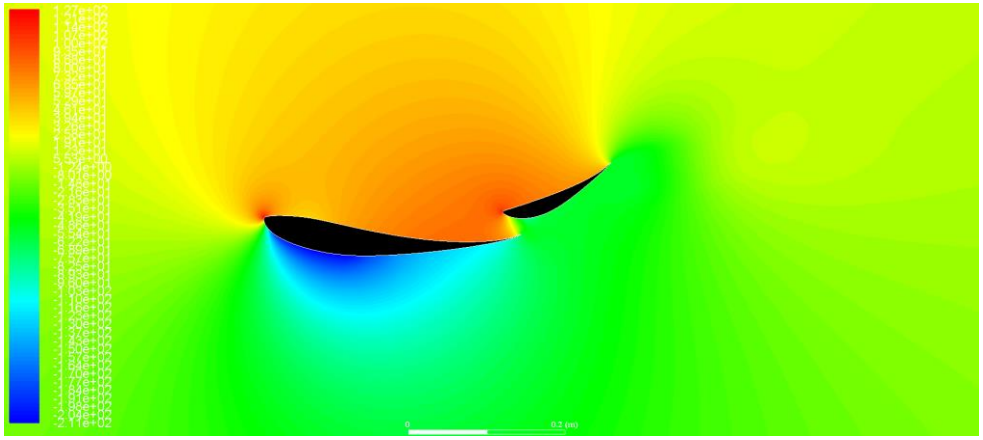

(b) Optimized configuration without ground effect

Figure 43 Static pressure contours of optimized configuration with and without ground effect

Figure 44 shows the possible schematic of a 3D extrusion of the 2D optimized two-element configuration described in Section 4.6 that can be incorporated in a 3D CAD model of the 2019 WashU Racing race car. In order for the wing to fit at its current height, some changes to the forward frame geometry and nosecone would have to be made to package it properly. As much lateral space as the rules allow should be exploited to increase the span of the wing (to the outside of the front tires). This wing in its current position reaches a height of 0.182 m above the front wheels; it could be advisable to scale the combined c of the two-element configuration until it reaches a height of 0.25 m above the ground in front of the front tires. Such an increase in c would allow for additional downforce generation by the front wing and could be easily implemented if higher downforce is desired to benefit the performance of the car.

For all practical purposes, it might be prudent to be conservative regarding the actual wing locations in terms of the values of H1, H2, and H3. The vehicle goes through several dynamic maneuvers during its time on the track; therefore it would be good to investigate the changes in ground height during acceleration, braking, and turning. Since there are significant decreases in negative lift generation once flow separates from the flap, it might be a good idea to choose a lower value than the suggested by the optimal configuration, allowing for the optimal configuration to occur only during the most extreme case of the vehicle movement. This way, there will be less unexpected pressure changes and the driver can predict the handling characteristics of the vehicle in a better manner. When choosing an optimal configuration for actual use in Formula SAE, there are more constraints than there are when the only goal is to maximize the downforce for a set of conditions.

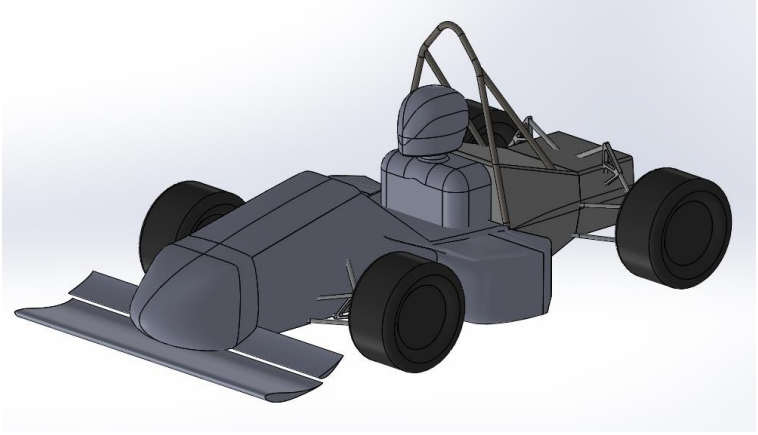

(a) Isometric view, 3D CAD model with front wing

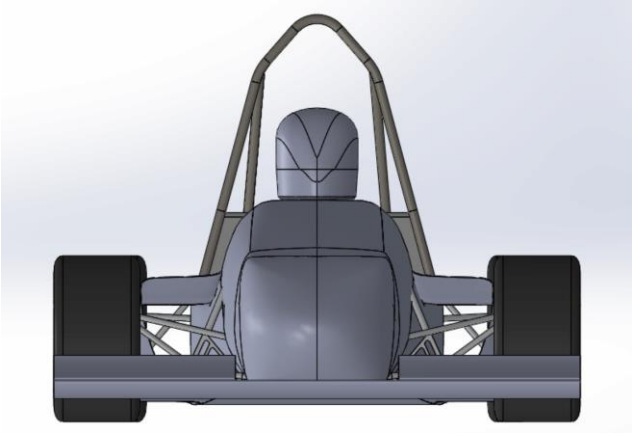

(b) Front view, 3D CAD model with front wing

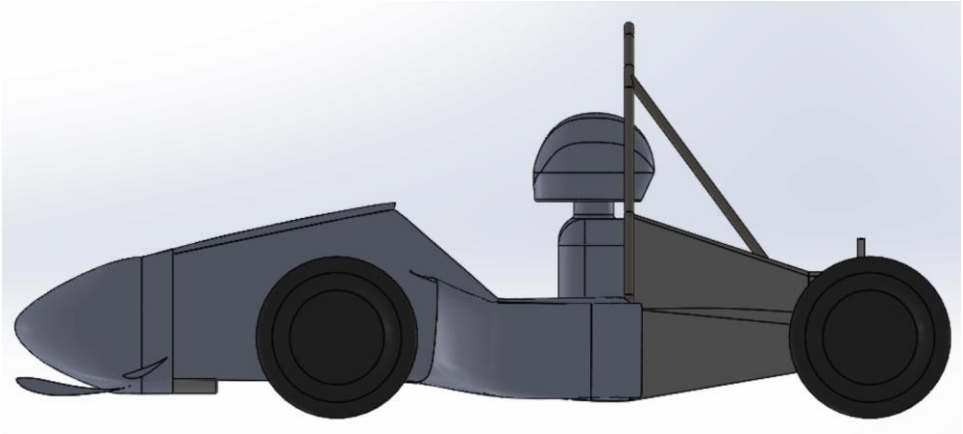

(c) Front view, 3D CAD model with front wing

Figure 44 Views of 3D front wing geometry on CAD race car model

Chapter 5

Conclusions and Future Work

An important issue for front wing design of a Formula SAE race car is that there is not enough published experimental data for inverted two element airfoils/wings at low speeds, in close proximity to the ground. Formula 1 cars travel at much faster speeds and have much larger size than a FSAE car; therefore, the designs used for Formula 1 cars may not be the most optimal configurations for a FSAE car. This study provides a fundamental understanding on how a variety of high lift airfoils behave at various angles of attack in close proximity to the ground as well as how an airfoil at a single α behaves at various heights above the ground. This thesis has clearly demonstrated the choice of the S1210 as the main element and FX74 as the flap to create a superior two-element wing configuration for a FSAE car having a $-C_L = 4.263$. The specifics on this optimal configuration can be found in Section 4.6 of this thesis.

A recommendation for future work is to design a rear wing that should be modelled with at least two elements to balance the car's center of pressure between the front and rear axles of the chassis. It is imperative to balance the center of pressure relative to the center of mass of the vehicle and recognize that pushing the center of pressure rearward of the center of mass will create a potentially desirable oversteer effect. In addition, the front or rear wing configurations may be optimized using optimization tools such as the genetic algorithm to assist in finding a global maximum negative lift value, versus using a gradient based optimization approach as is

used in this thesis. Gurney flaps can also be added to the front or rear wing geometries to further generate downforce (at the expense of more drag). These designs can also be transferred into 3D to study the difference between 2D and 3D CFD simulations. For a 3D model, end-plates can be tailored to minimize bleed of high-pressure air from the side of the car to under the front wing. A challenging problem could be the addition of the rotating front wheels to see how they affect the downforce generated by the front wing.

References

[1] SAE International “2017-18 Formula SAE® Rules,” FSAE Online, https://www.fsaeonline.com/content/2017-18-FSAE-Rules-091317.pdf.

[2] Abbott, I. H. A. and von Doenhoff, A. E., *Theory of Wing Sections: Including a Summary of Airfoil Data*, New York: Dover Publications, 1957.

[3] Zerihan, J. and Zhang, X., “Aerodynamics of a Single Element Wing in Ground Effect”, Journal of Aircraft, Vol. 37, 2000, pp. 1058-1064, DoI: 10.2514/2.2711.

[4] Zhang, X. and Zerihan, J., “Aerodynamics of a Double-Element Wing in Ground Effect”, AIAA Journal, Vol. 41, 2003, pp.1007-1016, DoI: 10.2514/2.2057.

[5] Mahon, S. and Zhang, X., “Computational Analysis of an Inverted Double Element Airfoil in Ground Effect”, Journal of Fluids Engineering, Vol. 128, No. 6, 2006, pp. 1172-1180, DoI: 10.1115/1.2353268.

[6] Mcbeath, S., *Competition Car Aerodynamics*, Veloce Publishing Ltd, 2017.

[7] UIUC Applied Aerodynamics Group, “UIUC Airfoil Coordinates Database,” UIUC Airfoil Data Site, m-selig.ae.illinois.edu/ads/coord_database.html.

[8] CFD Online, “Y plus wall distance estimation,” 2011, https://www.cfd-online.com/Wiki/Y_plus_wall_distance_estimation

[9] ANSYS Inc., “ANSYS 12.0 User Manual”, 2012.

[10] Qu, Q., Zuo, P., Qin, Y., Liu, P., and Agarwal, R. K., “Numerical Investigation of the Aerodynamics of an Inverted Three-Element Airfoil in Ground Effect for Race Car Application”, 34th AIAA Applied Aerodynamics Conference, 2016, DoI: 10.2514/6.2016-4180.

[11] Smith, A.M.O, “High-Lift Aerodynamics,” 37th Wright Bothers Lecture, Journal of Aircraft, Vol. 12, No. 6, 1975, pp. 501-530, DoI: 10.2514/3.59830.

Appendix A

Airfoil Coordinates

Appendix A shows the x and y coordinate points for the geometries of all five high lift airfoils.

The coordinate points can be found at the UIUC Airfoil Coordinate Database [7].

A.1 CH10 Coordinates

X	Y
1.00000	0.00005
0.99754	0.00169
0.99070	0.00579
0.98037	0.01111
0.96698	0.01721
0.95044	0.02452
0.93064	0.03317
0.90775	0.04292
0.88202	0.05367
0.85370	0.06522
0.82309	0.07725
0.79048	0.08942
0.75616	0.10143
0.72043	0.11298
0.68359	0.12384
0.64594	0.13374
0.60778	0.14243
0.56937	0.14970
0.53099	0.15538
0.49265	0.15942
0.45435	0.16176
0.41638	0.16240
0.37887	0.16133
0.34204	0.15862
0.30609	0.15434
0.27120	0.14859
0.23760	0.14148
0.20549	0.13310
0.17504	0.12355
0.14648	0.11291
0.11999	0.10132
0.09576	0.08896

0.07395	0.07611
0.05468	0.06312
0.03811	0.05032
0.02433	0.03793
0.01338	0.02615
0.00548	0.01531
0.00098	0.00586
0.00000	0.00014
0.00098	-0.00450
0.00548	-0.00914
0.01338	-0.01179
0.02433	-0.01269
0.03811	-0.01209
0.05468	-0.01028
0.07395	-0.00759
0.09576	-0.00435
0.11999	-0.00076
0.14648	0.00320
0.17504	0.00748
0.20549	0.01201
0.23760	0.01667
0.27120	0.02136
0.30609	0.02597
0.34204	0.03040
0.37887	0.03457
0.41638	0.03839
0.45435	0.04178
0.49265	0.04466
0.53099	0.04693
0.56937	0.04851
0.60778	0.04933
0.64594	0.04932
0.68359	0.04845
0.72043	0.04672
0.75616	0.04423
0.79048	0.04108
0.82309	0.03739
0.85370	0.03322
0.88202	0.02867
0.90775	0.02386
0.93064	0.01896
0.95044	0.01410
0.96698	0.00936
0.98037	0.00516
0.99070	0.00212
0.99754	0.00044
1.00000	-0.00006

A.2 E423 Coordinates

X	Y
1.00000	0.00000
0.99655	0.00159
0.98706	0.00650
0.97304	0.01434
0.95530	0.02381
0.93358	0.03376
0.90734	0.04400
0.87671	0.05481
0.84221	0.06620
0.80436	0.07803
0.76373	0.09010
0.72090	0.10215
0.67644	0.11391
0.63092	0.12506
0.58491	0.13524
0.53893	0.14410
0.49347	0.15116
0.44870	0.15593
0.40464	0.15828
0.36149	0.15824
0.31947	0.15590
0.27885	0.15138
0.23987	0.14485
0.20286	0.13657
0.16816	0.12676
0.13611	0.11562
0.10700	0.10337
0.08106	0.09023
0.05852	0.07646
0.03953	0.06232
0.02421	0.04812
0.01262	0.03419
0.00481	0.02093
0.00071	0.00879
0.00002	0.00088
0.00033	-0.00192
0.00071	-0.00362
0.00125	-0.00518
0.00157	-0.00590
0.00194	-0.00656
0.00237	-0.00717
0.00288	-0.00771
0.00348	-0.00823
0.00415	-0.00874
0.00571	-0.00969
0.00751	-0.01057
0.01065	-0.01177
0.01365	-0.01266
0.02892	-0.01485
0.04947	-0.01482
0.07533	-0.01236

0.10670	-0.00740
0.14385	-0.00002
0.18727	0.00922
0.23688	0.01913
0.29196	0.02865
0.35163	0.03687
0.41449	0.04283
0.47867	0.04626
0.54275	0.04760
0.60579	0.04715
0.66690	0.04501
0.72503	0.04126
0.77912	0.03625
0.82836	0.03050
0.87219	0.02444
0.91012	0.01844
0.94179	0.01286
0.96692	0.00794
0.98519	0.00390
0.99629	0.00106
1.00000	0.00000

A.3 FX74 Coordinates

X	Y
1.00000	0.00009
0.99754	0.00189
0.99070	0.00624
0.98037	0.01150
0.96698	0.01741
0.95044	0.02402
0.93064	0.03188
0.90775	0.04001
0.88202	0.04848
0.85370	0.05718
0.82309	0.06616
0.79048	0.07549
0.75616	0.08510
0.72043	0.09482
0.68359	0.10446
0.64594	0.11385
0.60778	0.12287
0.56937	0.13137
0.53099	0.13916
0.49265	0.14604
0.45435	0.15177
0.41638	0.15606
0.37887	0.15868
0.34204	0.15944
0.30609	0.15820
0.27120	0.15493
0.23760	0.14964

0.20549	0.14243
0.17504	0.13344
0.14648	0.12292
0.11999	0.11110
0.09576	0.09826
0.07395	0.08459
0.05468	0.07030
0.03811	0.05576
0.02433	0.04145
0.01338	0.02769
0.00548	0.01518
0.00098	0.00518
0.00000	-0.00021
0.00098	-0.00435
0.00548	-0.00787
0.01338	-0.00871
0.02433	-0.00754
0.03811	-0.00539
0.05468	-0.00292
0.07395	-0.00022
0.09576	0.00270
0.11999	0.00584
0.14648	0.00921
0.17504	0.01279
0.20549	0.01651
0.23760	0.02030
0.27120	0.02410
0.30609	0.02786
0.34204	0.03152
0.37887	0.03503
0.41638	0.03832
0.45435	0.04134
0.49265	0.04400
0.53099	0.04624
0.56937	0.04801
0.60778	0.04925
0.64594	0.04992
0.68359	0.04997
0.72043	0.04936
0.75616	0.04807
0.79048	0.04608
0.82309	0.04334
0.85370	0.03978
0.88202	0.03537
0.90775	0.03013
0.93064	0.02434
0.95044	0.01851
0.96698	0.01290
0.98037	0.00756
0.99070	0.00319
0.99754	0.00068
1.00000	-0.00003

A.4 LA5055 Coordinates

X	Y
0.000000	0.000000
0.012500	0.030600
0.025000	0.042600
0.037500	0.052800
0.050000	0.061100
0.075000	0.076900
0.100000	0.088000
0.150000	0.106500
0.200000	0.118500
0.250000	0.128700
0.300000	0.134300
0.350000	0.138900
0.400000	0.137000
0.450000	0.131500
0.500000	0.119400
0.550000	0.103700
0.600000	0.087000
0.650000	0.070400
0.700000	0.058300
0.750000	0.045400
0.800000	0.032400
0.850000	0.022200
0.900000	0.014800
0.950000	0.006500
1.000000	0.000000
0.000000	0.000000
0.012500	-0.025900
0.025000	-0.031500
0.037500	-0.032400
0.050000	-0.032400
0.075000	-0.031500
0.100000	-0.030600
0.150000	-0.028700
0.200000	-0.027800
0.250000	-0.025000
0.300000	-0.023100
0.350000	-0.020400
0.400000	-0.018500
0.450000	-0.014800
0.500000	-0.013900
0.550000	-0.012000
0.600000	-0.010200
0.650000	-0.008300
0.700000	-0.007400
0.750000	-0.005600
0.800000	-0.003700
0.850000	-0.001900
0.900000	-0.000900
0.950000	-0.000500
1.000000	0.000000

A.5 S1210 Coordinates

X	Y
1.00000	0.00000
0.99837	0.00101
0.99398	0.00397
0.98753	0.00832
0.97908	0.01317
0.96811	0.01811
0.95437	0.02328
0.93796	0.02874
0.91898	0.03443
0.89754	0.04032
0.87376	0.04637
0.84779	0.05254
0.81980	0.05879
0.78997	0.06506
0.75851	0.07130
0.72561	0.07747
0.69151	0.08349
0.65642	0.08932
0.62058	0.09490
0.58423	0.10016
0.54763	0.10505
0.51105	0.10948
0.47473	0.11335
0.43891	0.11653
0.40378	0.11892
0.36955	0.12046
0.33652	0.12091
0.30456	0.12000
0.27347	0.11784
0.24341	0.11462
0.21445	0.11047
0.18681	0.10556
0.16069	0.09994
0.13622	0.09362
0.11351	0.08672
0.09269	0.07932
0.07388	0.07149
0.05719	0.06332
0.04282	0.05484
0.03068	0.04593
0.02054	0.03672
0.01239	0.02755
0.00626	0.01866
0.00217	0.01030
0.00016	0.00277
0.00023	-0.00345
0.00337	-0.00773
0.01034	-0.01070
0.02071	-0.01324
0.03417	-0.01529
0.05052	-0.01685

0.06959	-0.01786
0.09118	-0.01830
0.11512	-0.01810
0.14119	-0.01715
0.16911	-0.01524
0.19906	-0.01183
0.23157	-0.00697
0.26670	-0.00124
0.30427	0.00504
0.34404	0.01158
0.38575	0.01814
0.42909	0.02446
0.47370	0.03032
0.51919	0.03551
0.56515	0.03986
0.61113	0.04320
0.65666	0.04543
0.70127	0.04646
0.74446	0.04625
0.78575	0.04479
0.82465	0.04214
0.86071	0.03837
0.89349	0.03364
0.92255	0.02809
0.94754	0.02192
0.96791	0.01530
0.98299	0.00890
0.99284	0.00390
0.99828	0.00095
1.00000	0.00000

Appendix B

Airfoil Simulation Data

Appendix B shows simulation data from the single and two-element airfoil configurations.

B.1 Single Element Airfoil Angle of Attack - Data

Chuch Hollinger CH-10

Airfoil	Height (m)	Angle (degrees)	drag coeff	lift coeff	l/d efficiency	neg_lift
CH10	0.106	0	0.043721102	-1.1112514	25.41682046	1.111251
CH10	0.106	3	0.063671195	-1.364112	21.42431911	1.364112
CH10	0.106	9	0.12186087	-1.6252945	13.33729605	1.625295
CH10	0.106	12	0.16316624	-1.6831729	10.31569337	1.683173
CH10	0.106	15	0.20874488	-1.7091814	8.187896153	1.709181

Eppler 423

Airfoil	Height (m)	Angle (degrees)	drag coeff	lift coeff	l/d efficiency	neg_lift
E423	0.106	0	0.036072187	-1.1866171	32.89562399	1.186617
E423	0.106	3	0.055927004	-1.4228144	25.44056177	1.422814
E423	0.106	6	0.076704748	-1.6583544	21.61997064	1.658354
E423	0.106	9	0.11521	-1.6623	14.42843503	1.6623
E423	0.106	12	0.16270194	-1.6946655	10.41576702	1.694666
E423	0.106	15	0.20659814	-1.6861966	8.161722076	1.686197

Wortmann FX74

FX74	Height (m)	Angle (degrees)	drag coeff	lift coeff	l/d efficiency	neg_lift
FX74	0.106	0	0.037976441	-1.3469781	35.46878182	1.346978
FX74	0.106	3	0.044482252	-1.8668296	41.96796511	1.86683
FX74	0.106	6	0.071799206	-1.9773171	27.53953992	1.977317
FX74	0.106	9	0.11770876	-1.8735125	15.91650868	1.873513
FX74	0.106	12	0.17014532	-1.5729104	9.244511692	1.57291
FX74	0.106	15	0.24421269	-1.5589268	6.383479908	1.558927

LA5055

LA5055	Height (m)	Angle (degrees)	drag coeff	lift coeff	l/d efficiency	neg_lift
LA5055	0.106	0	0.027006857	-0.62616579	23.18543731	0.626166
LA5055	0.106	3	0.049435646	-0.74057152	14.98051669	0.740572
LA5055	0.106	6	0.0734668	-0.81229215	11.05658815	0.812292
LA5055	0.106	9	0.098206251	-0.93812125	9.552561476	0.938121
LA5055	0.106	12	0.12736841	-1.070787	8.407006101	1.070787
LA5055	0.106	15	0.16152754	-1.1780396	7.29311918	1.17804

S1210

S1210	Height (m)	Angle (degrees)	drag coeff	lift coeff	l/d efficiency	neg_lift
S1210	0.106	0	0.025592766	-1.3259199	51.80838601	1.32592
S1210	0.106	3	0.034486017	-1.8130441	52.57331109	1.813044
S1210	0.106	6	0.051814531	-2.1603886	41.6946474	2.160389
S1210	0.106	9	0.087297323	-2.2532426	25.81113054	2.253243
S1210	0.106	12	0.13994563	-2.0713594	14.80117243	2.071359
S1210	0.106	15	0.20318393	-1.9163009	9.431360541	1.916301

B.2 Single Element Airfoil Height Above the Ground - Data

Wortmann FX74

	Height (m)	Height (in)	Angle (degrees)	drag coeff	lift coeff	l/d efficiency	neg_lift
FX74	0.0127	0.5	6	0.16501547	-0.40218024	2.437227	0.40218
FX74	0.0254	1	6	0.1638015	-0.99352601	6.065427	0.993526
FX74	0.0508	2	6	0.1303058	-1.5852723	12.16578	1.585272
FX74	0.0889	3.5	6	0.086503241	-1.9136231	22.12198	1.913623
FX74	0.106	4.17	6	0.071799206	-1.9773171	27.53954	1.977317
FX74	0.127	5	6	0.0598558	-2.0311019	33.93325	2.031102
FX74	0.1524	6	6	0.050427551	-2.0297706	40.25122	2.029771
FX74	0.1778	7	6	0.044630893	-2.0042016	44.90615	2.004202
FX74	0.2286	9	6	0.038365522	-1.9564731	50.99561	1.956473
FX74	0.3048	12	6	0.03378274	-1.877165	55.5658	1.877165
FX74	0.6096	24	6	0.028474888	-1.733888	60.89183	1.733888
FX74	0.9144	36	6	0.027070835	-1.6828401	62.16432	1.68284

S1210

S1210	Height (m)	Height (in)	Angle (degrees)	drag coeff	lift coeff	l/d efficiency	neg_lift
S1210	0.0127	0.5	6	0.15663841	-1.349522	8.615524123	1.349522
S1210	0.0254	1	6	0.13819917	-1.7801606	12.88112367	1.7801606
S1210	0.0508	2	6	0.097828762	-2.087004	21.33323531	2.087004
S1210	0.0889	3.5	6	0.060541	-2.1867	36.11932409	2.1867
S1210	0.106	4.17	6	0.051752321	-2.1536988	41.61550165	2.1536988
S1210	0.127	5	6	0.044637984	-2.0880611	46.77767482	2.0880611
S1210	0.1524	6	6	0.039403472	-2.0169334	51.18669238	2.0169334
S1210	0.1778	7	6	0.036023717	-1.9544544	54.25465673	1.9544544
S1210	0.2286	9	6	0.032144012	-1.8574078	57.78394433	1.8574078
S1210	0.3048	12	6	0.029039921	-1.766144	60.8177963	1.766144
S1210	0.6096	24	6	0.025158699	-1.6224786	64.48976555	1.6224786
S1210	0.9144	36	6	0.024065922	-1.5749996	65.44522167	1.5749996

E423

E423	Height (m)	Height (in)	Angle (degrees)	drag coeff	lift coeff	l/d efficiency	neg_lift
E424	0.0127	0.5	6	0.15842325	-0.40692175	2.568573426	0.4069218
E425	0.0254	1	6	0.14828376	-1.0796693	7.281102799	1.0796693
E426	0.0508	2	6	0.12228207	-1.3740256	11.23652552	1.3740256
E427	0.0889	3.5	6	0.088274414	-1.5964369	18.08493342	1.5964369
E428	0.106	4.17	6	0.076704748	-1.6583544	21.61997064	1.6583544
E429	0.127	5	6	0.065585016	-1.7032229	25.96969558	1.7032229
E430	0.1524	6	6	0.056432237	-1.7331007	30.71118198	1.7331007
E431	0.1778	7	6	0.050138419	-1.7329875	34.56406354	1.7329875
E432	0.2286	9	6	0.042797898	-1.7059642	39.86093429	1.7059642
E433	0.3048	12	6	0.037560964	-1.6577116	44.1338939	1.6577116
E434	0.6096	24	6	0.0316529	-1.5528076	49.05735651	1.5528076
E435	0.9144	36	6	0.030143497	-1.5125776	50.17923435	1.5125776

B.3 Main Element Airfoil and Flap Pairing - Data

S1210, S1210

Main Height (m)	Main Angle (deg)	Slot Height (m)	Flap Angle (deg)	drag coeff	lift coeff	neg_lift	l/d efficiency
0.0508	6	0.015494	20	0.2564	-2.5910	2.5910	10.1073
0.0508	6	0.015494	30	0.3610	-2.7132	2.7132	7.5147
0.0508	6	0.015494	40	0.4702	-2.7521	2.7521	5.8530
0.0508	6	0.015494	50	0.4772	-2.8318	2.8318	5.9344

S1210, FX74

Main Height (m)	Main Angle (deg)	Slot Height (m)	Flap Angle (deg)	drag coeff	lift coeff	neg_lift	l/d efficiency
0.0508	6	0.015494	20	0.266	-2.498	2.498	9.406201312
0.0508	6	0.015494	30	0.369	-2.696	2.696	7.315260345
0.0508	6	0.015494	40	0.477	-2.798	2.798	5.867724419
0.0508	6	0.015494	42.5	0.408	-2.825	2.825	6.925912962
0.0508	6	0.015494	45	0.431	-2.853	2.853	6.622791922
0.0508	6	0.015494	50	0.476	-2.895	2.895	6.087586816

S1210, E423

Main Height (m)	Main Angle (deg)	Slot Height (m)	Flap Angle (deg)	drag coeff	lift coeff	neg_lift	l/d efficiency
0.0508	6	0.015494	20	0.2539	-2.4846	2.4846	9.7856
0.0508	6	0.015494	30	0.3712	-2.6582	2.6582	7.1603
0.0508	6	0.015494	40	0.4812	-2.6963	2.6963	5.6030
0.0508	6	0.015494	50	0.4845	-2.7213	2.7213	5.6165

B.4 Main Element Airfoil and Flap Angles of Attack - Data

S1210, FX74

Main Height (m)	Main Angle (deg)	Slot Height (m)	Flap Angle (deg)	drag coeff	lift coeff	neg_lift	l/d efficiency
0.0508	-6	0.016	20	0.146	-3.747	3.747	25.66438356
0.0508	-6	0.016	30	0.194	-2.529	2.529	13.03608247
0.0508	-6	0.016	40	0.270	-2.308	2.3077	8.547037037
0.0508	-6	0.016	50	0.365	-1.775	1.775	4.863013699
0.0508	-3	0.016	20	0.153	-3.819	3.819	24.96078431
0.0508	-3	0.016	25	0.192	-3.927	3.927	20.453125
0.0508	-3	0.016	30	0.236	-3.909	3.909	16.56355932
0.0508	-3	0.016	35	0.263	-3.331	3.331	12.66539924
0.0508	-3	0.016	40	0.287	-2.936	2.936	10.22996516
0.0508	-3	0.016	50	0.34	-2.736	2.736	8.047058824
0.0508	0	0.016	20	0.187	-3.423	3.423	18.30481283
0.0508	0	0.016	30	0.275	-3.564	3.564	12.96
0.0508	0	0.016	40	0.373	-3.500	3.5	9.383378016
0.0508	0	0.016	50	0.395	-3.084	3.084	7.807594937
0.0508	3	0.016	20	0.227	-2.921	2.921	12.86784141
0.0508	3	0.016	30	0.322	-3.047	3.047	9.462732919
0.0508	3	0.016	40	0.331	-2.968	2.968	8.966767372
0.0508	3	0.016	50	0.413	-3.057	3.057	7.401937046
0.0508	3	0.016	60	0.501	-3.044	3.044	6.075848303
0.0508	6	0.015494	20	0.266	-2.498	2.498	9.406201312
0.0508	6	0.015494	30	0.369	-2.696	2.696	7.315260345
0.0508	6	0.015494	40	0.477	-2.798	2.798	5.867724419
0.0508	6	0.015494	42.5	0.408	-2.825	2.825	6.925912962
0.0508	6	0.015494	45	0.431	-2.853	2.853	6.622791922
0.0508	6	0.015494	50	0.476	-2.895	2.895	6.087586816
0.0508	9	0.016	20	0.301	-2.185	2.185	7.259136213
0.0508	9	0.016	30	0.414	-2.409	2.409	5.81884058
0.0508	9	0.016	40	0.519	-2.472	2.472	4.76300578

B.5 Two Element Airfoil, Height H1 - Data

S1210, FX74

Main Height (m)	Main Angle (deg)	Slot Height (m)	Flap Angle (deg)	drag coeff	lift coeff	neg_lift	l/d efficiency
0.0381	-3	0.016	25	0.274	-3.434	3.434	12.53284672
0.0508	-3	0.016	25	0.192	-3.927	3.927	20.453125
0.0635	-3	0.016	25	0.161	-4.12	4.12	25.59006211
0.0762	-3	0.016	25	0.144	-2.441	2.441	16.95138889
0.0889	-3	0.016	25	0.131	-2.294	2.294	17.51145038
0.1016	-3	0.016	25	0.123	-2.253	2.253	18.31707317

B.6 Two Element Airfoil, Height H2 - Data

S1210, FX74

Main Height (m)	Main Angle (deg)	Slot Height (m)	Flap Angle (deg)	drag coeff	lift coeff	neg_lift	l/d efficiency
0.0635	-3	0.012	25	0.161	-3.952	3.952	24.54658
0.0635	-3	0.014	25	0.161	-4.064	4.064	25.24224
0.0635	-3	0.016	25	0.161	-4.120	4.12	25.59006
0.0635	-3	0.018	25	0.160	-4.168	4.168	26.05000
0.0635	-3	0.020	25	0.157	-4.223	4.223	26.89809
0.0635	-3	0.022	25	0.160	-3.072	3.072	19.20000
0.0635	-3	0.024	25	0.161	-2.786	2.786	17.30435
0.0635	-3	0.026	25	0.165	-2.533	2.533	15.35152
0.0635	-3	0.028	25	0.148	-2.300	2.3	15.54054
0.0508	6	0.008	50	0.550	-2.729	2.729	4.96182
0.0508	6	0.010	50	0.562	-2.771	2.771	4.93060
0.0508	6	0.012	50	0.573	-2.804	2.804	4.89354
0.0508	6	0.014	50	0.476	-2.884	2.884	6.05882
0.0508	6	0.016	50	0.475	-2.895	2.895	6.09474
0.0508	6	0.018	50	0.518	-3.048	3.048	5.88417

B.7 Two Element Airfoil, Height H3 - Data

S1210, FX74

Main Height (m)	Main Angle (deg)	Slot Height (m)	Flap Angle (deg)	drag coeff	lift coeff	neg_lift	l/d efficiency
0.0635	-3	-0.037	25	0.162	-3.908	3.908	24.12345679
0.0635	-3	-0.033	25	0.161	-4.015	4.015	24.9378882
0.0635	-3	-0.029	25	0.159	-4.121	4.121	25.91823899
0.0635	-3	-0.027	25	0.158	-4.179	4.179	26.44936709
0.0635	-3	-0.025	25	0.157	-4.223	4.223	26.89808917
0.0635	-3	-0.023	25	0.155	-4.263	4.263	27.50322581
0.0635	-3	-0.021	25	0.168	-2.710	2.71	16.13095238
0.0635	-3	-0.019	25	0.171	-2.748	2.748	16.07017544
0.0635	-3	-0.017	25	0.174	-2.767	2.767	15.90229885
0.0635	-3	-0.013	25	0.178	-2.781	2.781	15.62359551
0.0508	6	-0.024	50	0.474	-3.130	3.13	6.603375527
0.0508	6	-0.020	50	0.478	-3.139	3.139	6.566945607
0.0508	6	-0.016	50	0.480	-3.138	3.138	6.5375
0.0508	6	-0.012	50	0.512	-3.091	3.091	6.037109375
0.0508	6	-0.008	50	0.518	-3.048	3.048	5.884169884
0.0508	6	-0.004	50	0.509	-2.929	2.929	5.754420432
0.0508	6	0.000	50	0.508	-2.877	2.877	5.663385827

Vita

Michael Grabis

Degrees M.S. Aerospace Engineering, Washington University in St. Louis, August 2019

B.S. Mechanical Engineering, Washington University in St. Louis, May 2018

Professional Societies Society of Automotive Engineers (SAE)

American Institute of Aeronautics and Astronautics (AIAA)

Publications Grabis, M. and Agarwal, R. K., "Computational Fluid Dynamics Analysis of Inverted Multi-Element Airfoils in Ground Effect", AIAA Scitech Forum and Exposition, San Diego, 7-11 January 2019, AIAA 2019-1336, DoI: 10.2514/6.2019-1336